Title
Micro-MRI and Metabolism Studies of Benign and Malignant Living Human Prostate Tissue

Author
Bancroft Brown, Jeremy

Publication Date
2018

Peer reviewed|Thesis/dissertation

Micro-MRI and Metabolism Studies of Benign and Malignant Living Human Prostate Tissue

by

Jeremy Bancroft Brown

DISSERTATION

Submitted in partial satisfaction of the requirements for degree of

DOCTOR OF PHILOSOPHY

in

Bioengineering

in the

GRADUATE DIVISION

of the

UNIVERSITY OF CALIFORNIA, SAN FRANCISCO

AND

UNIVERSITY OF CALIFORNIA, BERKELEY

Approved:

DocuSigned by:
John Kurhanewicz — John Kurhanewicz
593BD10CA23A498...
Chair

DocuSigned by:
Shuvo Roy — Shuvo Roy

DocuSigned by:
Jane Wang — Jane Wang

DocuSigned by:
Steven Conolly — Steven Conolly
822ED0E84B40494...

Committee Members

Acknowledgments

I am amazed to have been surrounded by so many phenomenal mentors and peers during my time in the Bioengineering graduate program at UCSF and UC Berkeley. My advisor, John Kurhanewicz, and my committee members, Shuvo Roy, Zhen (Jane) Wang, and Steven Conolly have been a key base of support. I am grateful to John for being a very supportive mentor who actively worked with me to develop a plan at every stage in the process. I must thank Shuvo for recognizing my potential to join the MSTP at UCSF and for teaching me the importance of independently applying for funding at an early stage in one's training. Jane always provided insightful feedback, and truly modeled the role of the physician-scientist. Early on in my training, Steve taught me numerous theoretical aspects of RF engineering and was instrumental with timely advice and resources.

Numerous colleagues from UCSF and UC Berkeley provided crucial expertise during my PhD. Alex Heller, now at Northwestern University, is a mechanical engineering mastermind full of fantastic ideas. Mozziyar Etemadi, also of Northwestern University, is particularly adept at selecting the best design from a range of options. Philip Chung, still at UCSF, has been a good friend and curious partner in conversation. Anita Flynn of UC Berkeley and Lucas Carvajal of UCSF taught me numerous practical aspects of RF engineering and I simply could not have built successful RF coils without them. Mark VanCriekinge and Subramaniam Sukumar of UCSF patiently mentored me in many aspects of NMR and MRI hardware and pulse sequences. Similarly, Peder Larson, Jeremy Gordon, and Susan Noworolski provided invaluable guidance on pulse sequence optimization.

During the later stages of my PhD, I benefited from considerable input from Renuka Sriram and Jinny Sun, both of the Kurhanewicz lab (Figure Acknowledgments.1), who are deeply knowledgeable about metabolic labeling, tissue culture studies, and 2D NMR pulse sequences. Romelyn Delos Santos played a critical role in multiple aspects of tissue handling and processing, frequently on weekends as well as weekdays. Rosalie Nolley of Stanford University was also an essential member of our team and a pleasure to work with, and graciously tolerated my presence at Stanford on one very long day of experiments. The advice of Donna Peehl of Stanford and UCSF was also essential. Dr. Rahul Aggarwal of UCSF Urologic Oncology mentored me both in the clinical setting and in the process of grant-writing.

Figure Acknowledgments.1. The coolest lab-mates a person can have.

The UCSF Radiology and Urology teams were always a very patient and welcoming presence when I collected clinical tissue samples. I especially wish to thank Justin Delos Santos, Vahid Ravanfar, Fariba Ravanfar, and Christine Larson of UCSF Radiology and Biomedical Imaging. I'm also grateful to Dr. Katsuto Shinohara, Dr. Hao Nguyen, and Dr. Matthew Cooperberg of the UCSF Department of Urology and the vocational nurses Selvi Johnson, Yanira Rafael, Trinidad Gleave, and Jasmine Meidinger. Karen Lopez and Erica Oropeza of the UCSF Biobank were a pleasure to work with as well, and Dr. Zoe Laura Tabatabai and Dr. Jeff Simko of the UCSF Department of Pathology tirelessly interpreted our pathology specimens. I also wish to thank the patients who donated their samples, who were always highly supportive of our research and who were so enjoyable to meet and converse with.

Figure Acknowledgments.2. The UCSF MSTP in full force.

The UCSF MSTP (Figure Acknowledgments.2) is an incredible program with a brilliant group of students. In this space I couldn't possibly recognize everyone in the program who inspired me and shaped how I now think about biology and medicine, but I'd like to thank Mark Anderson, Kevin Shannon, Geri Ehle, Amanda Andonian, Jana Toutolmin, and Catherine Norton for their key roles in assembling and maintaining this world-class program.

I would not have pursued a PhD in the field of MRI and prostate cancer without the incredible early mentoring I received from Professor Maryellen Giger, Professor Patrick LaRiviere, Professor Hui Li, Li Lan, and others in the University of Chicago Department of Radiology. During my undergraduate years, the Giger lab at UChicago was like my second home, not to mention the place where I learned computer programming and machine learning, and for that I am eternally grateful.

Frank Wen and Vladislav Petkov from the University of Chicago are the two brilliant individuals that I have been lucky to call close friends, and I can always learn something new from them, whether that means traveling in a foreign country or simply enjoying a dissertation-level conversation over an expertly prepared (by them!) dinner.

My mother, Margery Bancroft, and my father David Brown, have always supported and believed in me without setting expectations. My grandparents Robert L. Bancroft and Marion Page Bancroft were also like parents to me, and set me on an academic path from an early age. My aunts and uncles Tim Bancroft, Julie Baer and Kate Bancroft have also been a wonderful source of support and encouragement. Finally, I wish to thank my partner Ranna Khorram for her endless patience during my PhD and her thoughtfulness and optimism, as well as her amazing family.

Micro-MRI and Metabolism Studies of Benign and Malignant Living Human Prostate Tissue

Jeremy Bancroft Brown

Abstract

Prostate cancer is among the most prevalent and deadly of malignancies in both the United States and worldwide. Ongoing diagnostic challenges in prostate cancer include differentiating low-risk and high-risk tumors, and monitoring responses to therapy in patients with aggressive disease. Prostate cancer metabolism is characterized by a shift to aerobic glycolysis with lactate production and efflux, as well as increased tricarboxylic acid cycle activity, which has led to the investigation and development of metabolic imaging strategies such as hyperpolarized ^{13}C MRI. However, it is nontrivial to study human prostate cancer metabolism in vivo, and the capability to better characterize tumor metabolism from a variety of disease states would be valuable for metabolic imaging biomarker development. This dissertation focuses on developing ex vivo strategies to measure metabolism in benign and malignant living human prostate tissue. First, because prostate tissue heterogeneity can impact metabolic measurements, we present the engineering of a 600 MHz radiofrequency (RF) microcoil to assess the heterogeneity of freshly acquired human prostate biopsies using microscale diffusion-weighted imaging (DWI). Next, we demonstrate the capability of micro-DWI to determine the biopsy percentage of glandular tissue, setting the stage for establishing the percentage and grade of cancer using this approach. After this, we develop a protocol for nuclear magnetic resonance (NMR) quantification of lactate

production and efflux and glutamate fractional enrichment in freshly acquired living human prostate biopsies cultured with [1,6-$^{13}C_2$]glucose. In this study we demonstrate a significantly higher lactate efflux rate coming from low-grade prostate cancer versus benign biopsies in an early-stage patient population. This sets the stage for studies of metabolic fluxes and steady-state metabolite levels in biopsies from patients with aggressive disease before and after non-surgical therapy. Finally, due to recent interest in the potential role of Myc amplification and glutaminolysis upregulation in treatment insensitive castrate-resistant prostate cancer (CRPC) and neuroendocrine prostate cancer (NEPC), we present metabolic labeling results from a study of primary human prostate tissue slice cultures (TSCs) obtained at surgery and cultured with either [1,6-$^{13}C_2$]glucose or [3-^{13}C]glutamine. Our results are consistent with prior thinking on the role of glucose and glutamine metabolism in treatment-naïve prostate cancer.

Table of Contents

List of Figures

List of Tables

Introduction

Prostate cancer is among the most prevalent and deadly of malignancies in both the United States and worldwide, with 164,690 new cases and 29,430 estimated deaths in the United States in 2018.[1] Ongoing diagnostic challenges in prostate cancer include differentiating low-risk and high-risk tumors,[2,3,4,5] and monitoring responses to therapy in patients with aggressive disease.[6] Prostate cancer metabolism is characterized by a shift to aerobic glycolysis and lactate production,[7,8,9,10,11] which has led to the investigation and development of metabolic imaging strategies such as hyperpolarized ^{13}C MRI.[12,13,14,15,16] However, it is not trivial to study human prostate cancer metabolism in vivo, and the capability to better characterize tumor metabolism from a variety of disease states would be valuable for metabolic imaging biomarker development.[17] Hence, this dissertation focuses on developing ex vivo strategies to measure metabolism in benign and malignant living human prostate tissue.

Prostate biopsies are of particular interest for this dissertation because they can be obtained from patients who are not candidates for radical prostatectomy, including patients with very high grade prostate cancer as well as patients whose tumors have escaped prior therapy, such as men with castrate-resistant prostate cancer (CRPC) and/or neuroendocrine prostate cancer (NEPC). Furthermore, prostate cancer biopsies can be obtained from metastatic sites such as liver and bone, which is crucial for understanding the pathobiology of lethal disease. However, the development of RF coils, optimized imaging and NMR spectroscopy protocols, optimized biopsy and surgical tissue acquisition, handling, and metabolic labeling protocols performed in this dissertation was accomplished using an early-stage population of patients at biopsy as

well as patients receiving surgery as their primary therapy. Extending the techniques described herein to aggressive primary and metastatic prostate cancer before and after therapy will be a key priority for future research in our laboratory.

In Chapter 1, because prostate tissue heterogeneity (i.e. the variety and differential organization of cell types at a microscopic level) can impact metabolic measurements,[18] we present the engineering of a 600 MHz radiofrequency (RF) microcoil to assess the heterogeneity of human prostate biopsies using microscale diffusion weighted imaging (DWI). We demonstrate that this RF microcoil achieves superior mass sensitivity compared to commercially available room temperature 5 mm NMR probes.

In Chapter 2, we test the micro-DWI technique on a series of freshly acquired human biopsy samples and we demonstrate the capability of the 10^{th} percentile water apparent diffusion coefficient (ADC) value[19] to predict the biopsy percentage of glandular tissue determined by a board-certified genitourinary pathologist, setting the stage for establishing the percentage and grade of cancer using this approach.

In Chapter 3, we develop a protocol for nuclear magnetic resonance (NMR) quantification of lactate production and efflux and glutamate fractional enrichment in freshly acquired living human prostate biopsies cultured with [1,6-$^{13}C_2$]glucose. In this study, we show for the first time that we can study metabolic fluxes as well as steady-state metabolite levels from freshly acquired patient-derived biopsies, and we demonstrate a significantly higher rate of lactate efflux coming from low-grade prostate cancer versus benign biopsies in a early-stage patient population.

In Chapter 4, due to recent interest in the potential role of Myc amplification[20,21] and potentially glutaminolysis upregulation[22,23] in advanced disease such as treatment insensitive CRPC and/or NEPC, we present metabolic labeling results from a study of treatment-naïve primary human prostate tissue slice cultures (TSCs) cultured with either [1,6-$^{13}C_2$]glucose or [3-^{13}C]glutamine. Our results are consistent with prior thinking on the role of glucose and tricarboxylic acid (TCA) cycle metabolism in prostate cancer, and set the stage for future studies in CRPC and NEPC tissue slices.

Chapter 1. Engineering of a 600 MHz RF Microcoil for Single-Biopsy Micro-Diffusion Weighted Imaging

Magnetic resonance imaging (MRI) and nuclear magnetic resonance (NMR) have an intrinsically low signal-to-noise ratio (SNR) originating from the small magnitude of the magnetic Hamiltonian $-\boldsymbol{\mu} \cdot \mathbf{B}_0$ relative to $k_B T$, the thermal energy.[24] This has motivated creative strategies to increase SNR such as using higher static magnetic fields, cryogenic cooling of the sample and/or radiofrequency (RF) coil,[25] polarization transfer approaches,[26] and even hyperpolarization of the sample using millimeter waves under cryogenic temperatures and high magnetic fields.[24,27] It is also possible to increase SNR using miniaturized RF coils that feature increased magnetic coupling to the sample.[28] In this study, we set out to develop a device that could measure the cellularity of a single prostate biopsy in an ex vivo setting using diffusion-weighted imaging (DWI). Given the small dimensions and weight of a single 18-gauge prostate biopsy (0.4 mm × 5-15 mm, 3 to 6 mg), we chose to construct a 600 MHz RF microcoil that could provide high sensitivity for ^{1}H imaging of small samples at 14 tesla.

Theory

Signal considerations. There are three fundamental equations that govern the magnetic behavior of RF coils: Ampere's law, Faraday's law, and the reciprocity principle. Ampere's law (shown below in a simplified form for an infinite wire) states that the magnetic field generated by a current-carrying wire is proportional to $1/r$, meaning that the magnetic field will be stronger if the sample is closer to the wire.

Ampere's law:

$$\mathbf{B}(r) = \frac{\mu_0 I}{2\pi r}\hat{\theta} \qquad (1.1)$$

Meanwhile, Faraday's law states that during signal reception, the coil voltage is proportional to the time derivative of the magnetic flux that the sample produces within the RF coil.

Faraday's law:

$$\mathcal{E} = -\frac{d\Phi}{dt} \qquad (1.2)$$

Finally, the reciprocity principle[29,30,31,32] exploits the hidden relationship between Ampere's law and Faraday's law to summarize the RF coil voltage during reception in terms of the transmission $\mathbf{B}_1$ field and the precessing sample magnetization, **M**.

Reciprocity principle:

$$\mathcal{E} = -\int \frac{\partial}{\partial t}\left(\mathbf{B_1} \cdot \mathbf{M}\right) dV \qquad (1.3)$$

The immediate consequence of the reciprocity principle is that if the coil is very close to the sample, it can deliver a higher $\mathbf{B}_1$ and therefore receive a much higher signal in response to the same sample magnetization **M**. (This is true even for coils operated in receive-only mode.) Therefore, given the goal of imaging individual biopsy samples, it made sense to construct a miniaturized RF coil that was geometrically optimized for signal reception from small samples.

Noise considerations. The signal considerations described above may be divided by noise to yield an expression[31,32] for the signal-to-noise-ratio (SNR).

Signal-to-noise ratio:

$$\text{SNR} \propto \left[\frac{1}{F}\right] \left[\frac{\omega_0 \int \left(\frac{\mathbf{B}_{10+}}{i} \cdot \mathbf{M}_{xy,\,\text{max}}\right) dV}{\sqrt{4k_\text{B}\left(T_s \int \sigma(\mathbf{r}) \left|\frac{\mathbf{E}(\mathbf{r})}{i}\right|^2 dV + T_c R_c\right) \Delta f}}\right] \qquad (1.4)$$

The net signal-to-noise ratio of an RF receive chain is typically dominated by three factors, namely the sample, the coil circuit, and the preamplifier. In this equation, F describes the degradation of the SNR by the preamplifier. (Past the preamplifier, the signal amplitude is so large as to be nearly impervious to thermal electronic noise.) In the numerator, we see the reciprocity principle with the time derivative performed, which makes explicit the signal dependence on the precession frequency ω_0, which is determined by the magnetic field strength and the gyromagnetic ratio. In the denominator, we see a complicated expression for RF noise (Johnson-Nyquist noise). First, it should be noted that RF noise is proportional to sqrt(Δf), the reception bandwidth determined by the analog-to-digital converter (ADC) settings.[24,30] Second, we observe that the noise expression contains two terms. The first term beginning with T_s is known as sample noise and is proportional to the sample temperature.[32] It consists of a volume integral of the sample conductivity multiplied by the square of the electric field generated by the RF coil. In biological samples with high ionic content, the conductivity and therefore sample noise can be substantial. The second term beginning with T_c is known as coil noise and is proportional to the coil temperature.[32] If the sample noise term is larger, the SNR is said to be sample noise dominated,[30] whereas if the coil noise term is larger, the SNR is said to be coil noise dominated. RF microcoils are typically, but not always, coil-noise dominated due to the small sample size. In this situation, the

choice of low-loss materials for the engineering of the RF coil and its associated circuit becomes critical for performance.

Quality factor. The quality factor (*Q*-factor) of an RF coil is defined as the ratio of energy that is inductively stored to energy that is resistively lost per cycle. Within a simple resonating circuit, it can also be described as the ratio of reactance (*X*) to resistance (*R*):

$$Q = \frac{X}{R} = \frac{\omega_0 L}{R} \qquad (1.5)$$

Using equations for the energy stored within the magnetic field, it is possible to relate the self-inductance *L* and coil current *i* to the magnetic field $\mathbf{B}_1$:

$$U = \frac{1}{2}Li^2 = \frac{1}{2}\mu_0 \int |\mathbf{B}_1|^2 dV \qquad (1.6)$$

$$L = \mu_0 \int \left| \frac{\mathbf{B}_1}{i} \right|^2 dV \qquad (1.7)$$

We can then describe the Q-factor in terms of $\mathbf{B}_1$ and *R*:

$$Q = \frac{\omega_0 \mu_0}{R} \int \left| \frac{\mathbf{B}_1}{i} \right|^2 dV \qquad (1.8)$$

By comparing Eq. (1.8) to Eq. (1.4), we can observe:

$$\text{SNR} \propto \sqrt{Q}\sqrt{\omega_0} \qquad (1.9)$$

Therefore, the *Q*-factor is an important property of an RF coil because its square root is proportional to SNR.[29] Furthermore, sample noise as described in Eq. (1.4) increases the effective resistance of the coil circuit, denoted *R* in Eq. (1.8), which leads to the distinction between unloaded *Q* (when no sample is present) and loaded *Q* (when a sample is present).[32] However, it should be noted that the *Q*-factor does not

characterize the magnetic coupling of the coil to the sample, as described in Eq. (1.3), (1.4).

When measuring the *Q*-factor, the above definition of *Q*, Eq. (1.5) is often replaced by a more convenient formulation in terms of the bandwidth of the resonator. The bandwidth formulation is equivalent to Eq. (1.5) for large *Q* but should not be considered strictly equivalent.[33] Using the bandwidth formulation, the *Q*-factor of a tuned and matched RF coil (which includes the equivalent series resistance of any tuning and matching components) can be measured from a port reflection (S_{11}) measurement on a calibrated network analyzer using the equation[34]:

$$Q = \frac{2f_0}{\mathrm{BW}_{S_{11},-3\ \mathrm{dB}}} \qquad (1.10)$$

Where $\mathrm{BW}_{S_{11},-3\ \mathrm{dB}}$ is the -3 dB bandwidth of the negative-polarity S_{11} peak. However, this approach should be used cautiously if the tuning and matching network contains additional non-negligible inductances. In that case, the *Q*-factor measured from S_{11} might not equal the RF coil *Q*-factor that determines SNR. When in doubt, one should fall back upon a S_{21} measurement with the RF coil weakly inductively coupled to a small pickup coil. In that case, the following equation[34] should be used.

$$Q = \frac{f_0}{\mathrm{BW}_{S_{21},-3\ \mathrm{dB}}} \qquad (1.11)$$

For this study, we chose the S_{11} approach to avoid the challenge of designing a pickup coil suitable for probing a microcoil.

Materials and Methods

MRI scanner. The RF microcoil was designed for use with a Varian 600 MHz (14.1 T) small animal MRI system. The inner diameter of the system bore with gradients installed was 54 mm, and the inner diameter of imaging probes designed for use with the system was 40 mm. The maximum gradient strength at isocenter was 1 T/m or 100 gauss/cm. The system contained an imaging gradient set with *xy*-shims up to second order and *z*-shims up to third order. Consequently, higher-order shims were not available on the system.

Choice of sample geometry. It is possible to scan a biopsy sample in a stretched-out orientation or a "coiled/bunched" orientation. In high-resolution magic angle spinning (HR-MAS) studies of biopsy samples, the "coiled/bunched" orientation is commonly used because it reduces the sample to a very small volume that is comparatively straightforward to shim.[35] However, for this study we selected the stretched-out orientation to yield optimal correlation between imaging and histopathology.

Choice of coil geometry. The most commonly employed RF coil geometries include the circular loop, the planar solenoid, the helical solenoid, the Helmholtz coil, and the saddle coil. For a stretched-out biopsy sample, the helical solenoid, Helmholtz coil, and saddle coil offer RF magnetic field ($\mathbf{B}_1$) homogeneity over a long, narrow region. Of these options, the helical solenoid offers the highest theoretical sensitivity, but at the cost of the long axis of the coil being perpendicular to the *z*-axis of the MRI scanner. This has potential to create shimming difficulties. Consequently, we selected the saddle coil geometry.[36] which is commonly used in commercial high-field NMR probes precisely because it allows the long axis of the coil to align with the long axes of

both the sample and the NMR spectrometer. In this orientation, the main magnetic field ($\mathbf{B}_0$) homogeneity of the sample can be better optimized using *z*-shims.

Choice of coil materials. Solid-core copper wire offers near-optimal RF coil conductivity at a low price. Consequently, the most commonly-confronted issue in RF coil design is the choice of material to stabilize the coil. Above approximately 100 MHz, many popular materials, such as epoxy, are unacceptable for RF coil embedding because the dielectric losses are far too high. For the same reason, UV-visible cured stereolithography resins such as RC31 NanoCure (EnvisionTEC, Inc.) are not acceptable RF coil substrates. We tested several options and found that both glass and Kapton (polyimide) provided excellent performance. We ultimately settled upon Kapton due to its high durability as compared to glass. We found it was possible to procure Kapton tubes that are used in medical catheters (MicroLumen, Inc.). We used these tubes for a double purpose, as both a coil substrate and sample chamber.

Choice of susceptibility matching material. We chose to submerge the RF coil in Fluorinert FC-40 (Sigma-Aldrich, Inc), a ^{1}H MRI-invisible fluorinated hydrocarbon. This eliminated air in the region of the sample and made the sample much easier to shim. The point where the RF coil leads exited the chamber containing the FC-40 was sealed with dental acrylic.

Choice of coil adhesives. Any adhesive bonded to an RF coil becomes part of the circuit and contributes to coil losses. After testing several adhesives, we determined that two-component dental acrylic (frequently used to fabricate retainers) provided the best RF performance.[32] However, close to the sample volume, small air bubbles in the cured acrylic can contribute to $\mathbf{B}_0$ inhomogeneity, which is a significant problem in high-field

MRI. Therefore, our final design only made use of the dental acrylic far away from the sample volume, to seal the chamber containing the susceptibility-matching fluid.

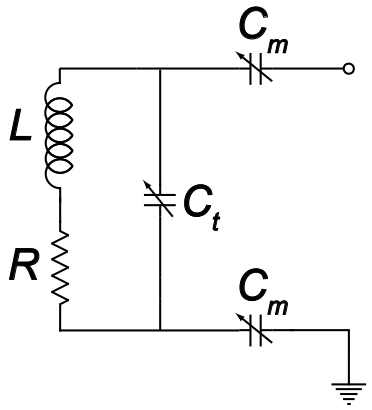

Figure 1.1. Tuning and matching network.

Choice of tuning and matching circuit topology.

The optimal tuning and matching circuit converts the RF coil impedance to 50 Ω, and also allows the coil to operate in balanced (differential) mode, which provides optimal energy transfer to and from the magnetic component of the RF field ($\mathbf{B}_1$). Given these constraints, we selected a very simple three-component balanced tuning and matching circuit (Figure 1.1), which is capable of transforming inductive loads to 50 Ω real impedance while injecting a minimum of noise into the RF coil circuit.

Symbolic solution to the tuning and matching network.

Tuning and matching condition:

$$\Re[Z] = 50,\ \Im[Z] = 0 \tag{1.12}$$

Network impedance:

$$Z = Z_l || Z_t + 2Z_m = \frac{1}{\frac{1}{Z_l} + \frac{1}{Z_t}} + 2Z_m \tag{1.13}$$

Component impedances:

$$\begin{aligned} Z_l &= j\omega L + R \\ Z_t &= \frac{1}{j\omega C_t} + \frac{1}{Q_t \omega C_t} \\ Z_m &= \frac{1}{j\omega C_m} + \frac{1}{Q_m \omega C_m} \end{aligned} \tag{1.14}$$

Complex expansion of network impedance:

$$D \equiv C_m \omega \left(Q_t^2 \left(C_t^2 \omega^2 \left(L^2 \omega^2 + R^2 \right) - 2C_t L \omega^2 + 1 \right) + 2C_t Q_t R \omega + 1 \right) \tag{1.15}$$

$$\begin{aligned} \Re[Z] = \frac{1}{Q_m D} \big(& \omega^4 \left(C_m C_t L^2 Q_m Q_t + 2C_t^2 L^2 Q_t^2 \right) \\ & + \omega^2 \left(C_m C_t Q_m Q_t R^2 + 2C_t^2 Q_t^2 R^2 - 4C_t L Q_t^2 \right) \\ & + \omega \left(C_m Q_m Q_t^2 R + C_m Q_m R + 4C_t Q_t R \right) + \left(2Q_t^2 + 2 \right) \big) \end{aligned} \tag{1.16}$$

$$\Im[Z] = \frac{1}{D}\left(\omega^4\left(-C_m C_t L^2 Q_t^2 - 2C_t^2 L^2 Q_t^2\right)\right.$$
$$+\omega^2\left(-C_m C_t Q_t^2 R^2 + C_m L Q_t^2 + C_m L - 2C_t^2 Q_t^2 R^2 + 4C_t L Q_t^2\right) \quad (1.17)$$
$$\left.-4\omega(C_t Q_t R) + \left(-2Q_t^2 - 2\right)\right)$$

Given appropriate numerical values for L, R, Q_m and Q_t, the simultaneous equations Re[Z] = 50 and Im[Z] = 0 can be numerically solved for C_t and C_m using Eq. (1.15), (1.16), and (1.17). This process tends to be somewhat iterative because Q_m and Q_t are a function of the capacitor chosen, which is in turn a function of C_t and C_m.

Estimation of microcoil resistance. We decided to construct a saddle RF microcoil of approximately 2.2 mm inner diameter by 9 mm length using 24-gauge solid core copper wire (radius: 0.255 mm). For this coil geometry, the length of copper wire needed was 53 mm, including 3 mm for coil leads. The skin depth was estimated:

Skin depth:

$$\delta = \sqrt{\left(\frac{2\rho}{\mu}\right)\omega} \quad (1.18)$$

Where $\rho = 1.68\times10^{-8}$ Ω·m is the resistivity of copper, $\mu = (4\pi\times10^{-7})(1 - 0.78\text{ ppm})$ N·A^{-2} is the magnetic permeability of copper, and $\omega = 2\pi(600\times10^6)$ s^{-1}. Using the calculated skin depth value δ = 2.66 μm, it was possible to estimate the cross-sectional area of wire that contained flowing current, and in turn estimate the coil resistance:

Current area:

$$A = \pi r^2 - \pi(r-\delta)^2 \quad (1.19)$$

Coil resistance:

$$R = \frac{\rho l}{A} \quad (1.20)$$

from these relationships, we obtained R = 428 mΩ.

Estimation of microcoil inductance. Given the very weak dependence of RF coil inductance upon frequency, we chose to neglect this effect, and we estimated the coil inductance using a direct current (DC) simulation of saddle coil geometry within the ANSYS Maxwell finite element magnetostatic simulation software (ANSYS, Inc.). We obtained L = 32.27 nH (Figure 1.2).

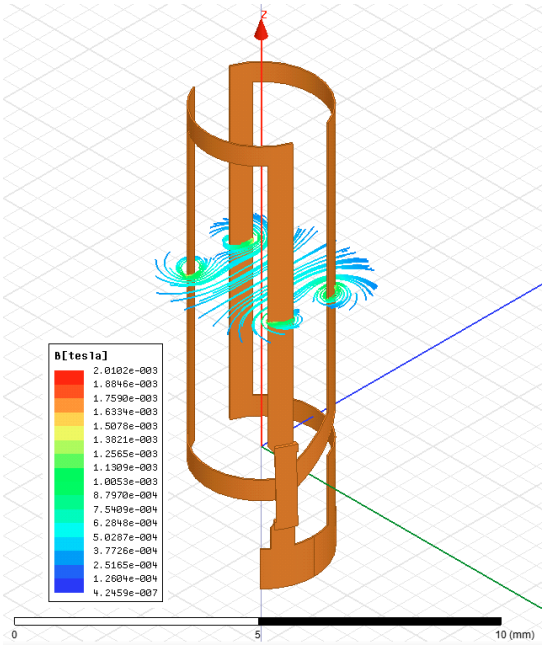

Figure 1.2. Simulation of microcoil inductance in ANSYS Maxwell.

Numerical solution of the tuning and matching circuit. Using R = 428 mΩ, L = 32.27 nH, and $Q_t = Q_m$ = 1250, with $\omega = 2\pi(600\times10^6)$ s^{-1}, we numerically solved the complex expansion of the network impedance to yield C_t = 1.95 pF and C_m = 0.45 pF.

Choice of tuning and matching circuit capacitors. We found that Johanson ThinTrim half-turn non-magnetic capacitors offered high Q-factors at a low price. The primary limitation of these capacitors was that they were very fragile and had to be stabilized securely on a rigid circuit board substrate. The Johanson 9701-0SL-1 provided an adjustable capacitance from 0.25 pF to 0.7 pF. We used the 9701-0SL-1 for both the tuning and matching capacitors, and we chose to use a high-Q non-magnetic chip capacitor close to the coil to add additional tuning capacitance.

Choice of tuning and matching substrate. The commonly-used inexpensive FR-4 circuit board material is unacceptable for RF coil design at higher frequencies due to its high dielectric loss tangent. Popular low-loss tangent substrates include Teflon (PTFE)

and Kapton. Consequently, we settled upon Rogers RT Duroid 5880, a PTFE-based laminate that was bonded to rolled 1 Oz copper. This material had excellent higher frequency RF performance and could easily be milled using a two-axis CNC router (Othermill, Bantam Tools, Inc.).

Choice of coaxial cable. Coaxial cable losses take place outside of the coil circuit and consequently are not as significant as losses within the coil circuit itself. However, in the interest of achieving optimal sensitivity we selected Micro-Coax 0.141 (Micro-Coax, Inc.) as a high-performance rigid coaxial option with a solid-core inner conductor, PTFE dielectric and solid copper shield. At 600 MHz, this choice provided estimated losses of 0.29 dB/m as compared to 0.53 dB/m for commonly-used RG-58.

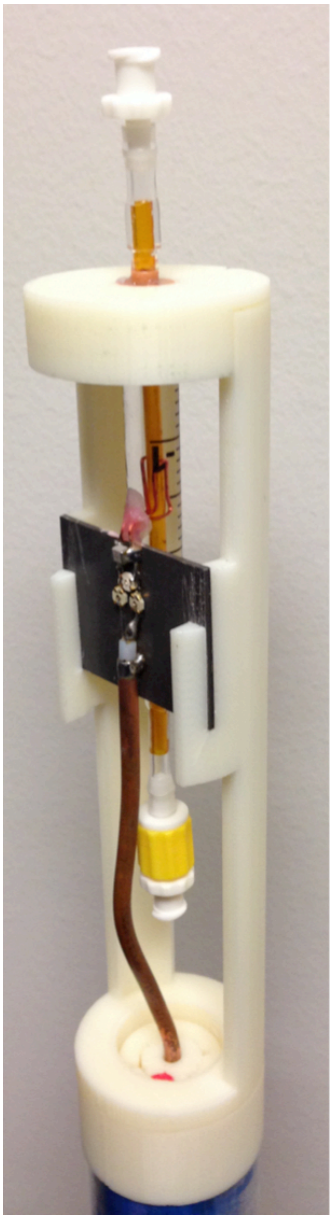

Figure 1.3. RF microcoil and housing.

Results

Construction of RF coil. The finalized ^{1}H saddle microcoil (Figure 1.3) was constructed from 24-gauge copper wire that was formed using a removable 3D-printed coil model (Perfactory 3, EnvisionTEC Inc.) and designed to tightly encircle a 2.2 mm outer diameter polyimide catheter (Part number 860-II, MicroLumen, Inc). The inner coil diameter was 2.2 mm and the length was 9 mm. The coil and the polyimide catheter were immersed in Fluorinert FC-40, which was contained within a polycarbonate pipette

tube. The point where the coil wires exited the tube was sealed using dental acrylic. The ends of the pipette tube were sealed using 3D-printed RC31 NanoCure inserts which were affixed using UV-cured glue. The polyimide catheter was sealed to Luer-lok fittings using PVC peristaltic pump tubing and UV-cured glue. The overall assembly was encased in a 3D-printed ABS housing suitable for insertion into a 40 mm inner diameter small-animal spectroscopy probe. The coil leads were soldered to a high-*Q* non-magnetic chip capacitor in parallel with a tuning and matching network consisting of Johanson ThinTrim 9701-0SL-1 capacitors soldered to Rogers RT Duroid 5880 substrate. The feed point of the tuning and matching network was directly soldered to Micro-Coax 0.141 cable, the shield of which was connected to a copper ground plane at the bottom of the microcoil housing.

Q-factor measurements of RF microcoil. The unloaded RF microcoil before placement in its full housing was easily impedance matched to 50 Ω, and the coil had a Q-factor of 270 computed from $Q = 2(BW)/f_0$, where *BW* was the –3 dB bandwidth of the S_{11} spectrum at 600 MHz measured using a network analyzer (Figure 1.4).

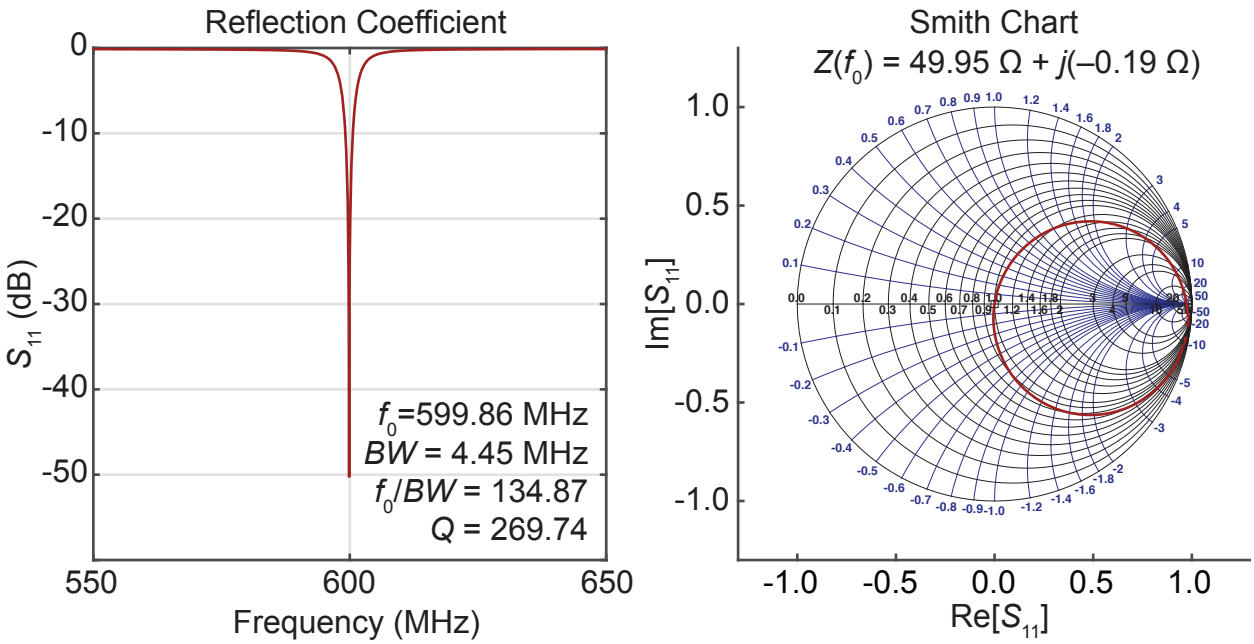

Figure 1.4. Network analyzer measurements of RF microcoil.

During the construction of the RF microcoil, we examined the *Q*-factor impact of the various structural components (Figure 1.5). When each coil component was added, the coil was tuned and matched, and the *Q*-factor was re-measured. As described above, the RF coil attached to its tuning and matching network on the Rogers RT Duroid 5880 substrate had a *Q*-factor of 270. Adding the acrylic seal (used for trapping the susceptibility-matching fluid Fluorinert FC-40) reduced the *Q*-factor to 238. Further adding the FC-40 to the coil chamber reduced

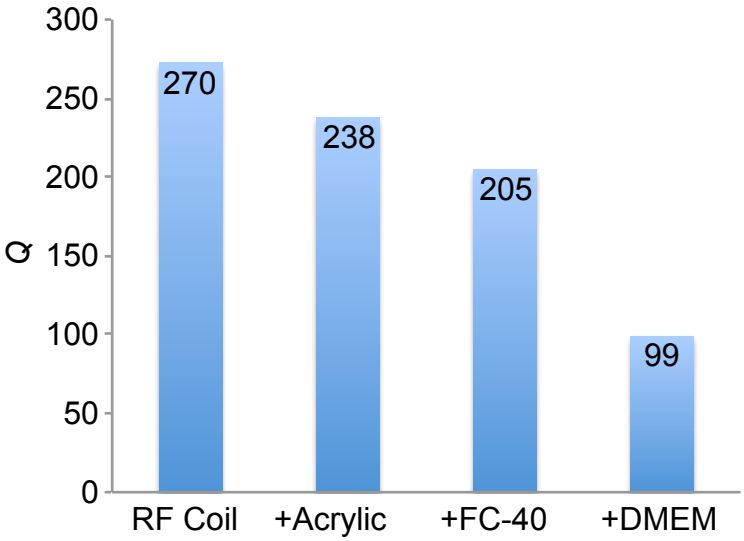

Figure 1.5. Impact of adding successive components on microcoil *Q*-factor.

the *Q*-factor to 205. However, adding Dulbecco's Modified Eagle Medium (DMEM) to the sample chamber had the most dramatic impact, reducing the *Q*-factor to 99. Given this *Q*-factor reduction, we concluded that the RF microcoil was in fact sample-noise dominated for high ionic content samples such as cell medium.

RF microcoil pulse width, lineshape and SNR. Using an H_2O sample, we observed considerable radiation damping[37] (Figure 1.6A). Consequently, the sample chamber was filled with a freshly opened D_2O / 0.05% trimethylsilylpropanoic acid (TSP) solution (Sigma-Aldrich, Inc.), and the RF microcoil was inserted into the Varian 600 (14.1 T) MRI scanner. Using TR = 15 seconds, the 90° RF pulse was found to equal 15 μs at 45 dBm (Figure 1.6B). The sample was automatically gradient shimmed, and the TSP lineshape and SNR were measured at a receiver gain of 10 dB using one transient with a 90° flip angle, 59,524 complex points, and a 3-second acquisition time (Figure 1.6C). The TSP lineshape was 2.17 / 14.94 / 17.49 Hz (50% / 0.55% / 0.11%) and the SNR, computed after matched apodization and using Eq. (1.21), was 608 / μmol ^{1}H (SNR = 608:1 per μmol of ^{1}H spins). The sensitive volume of the coil used for the SNR calculation was 38.3 μL, measured using a 2D gradient echo sequence (Figure 1.6D).

The SNR per μmol ^{1}H was computed using Eq. (1.21), with $\rho(D_2O)$ = 1.1044 g/mL and V_{coil} = 38.3 μL. Using MestreNova (MestreLab Research S.L) the SNR was computed from the ratio of the TSP peak height to the standard deviation of a large noise region that was upfield of 0 ppm. The SNR was computed after applying matched apodization (exponential line-broadening = 2.17 Hz = TSP full width at half maximum).

$$\frac{\text{SNR}}{\mu\text{mol }^1\text{H}} = \left(\frac{(10^6)(9)(0.0005)\rho(\text{D}_2\text{O})V_{\text{coil}}}{172.27\frac{\text{g}}{\text{mol}}}\right)^{-1} \text{SNR}_{\text{TSP}} \qquad (1.21)$$

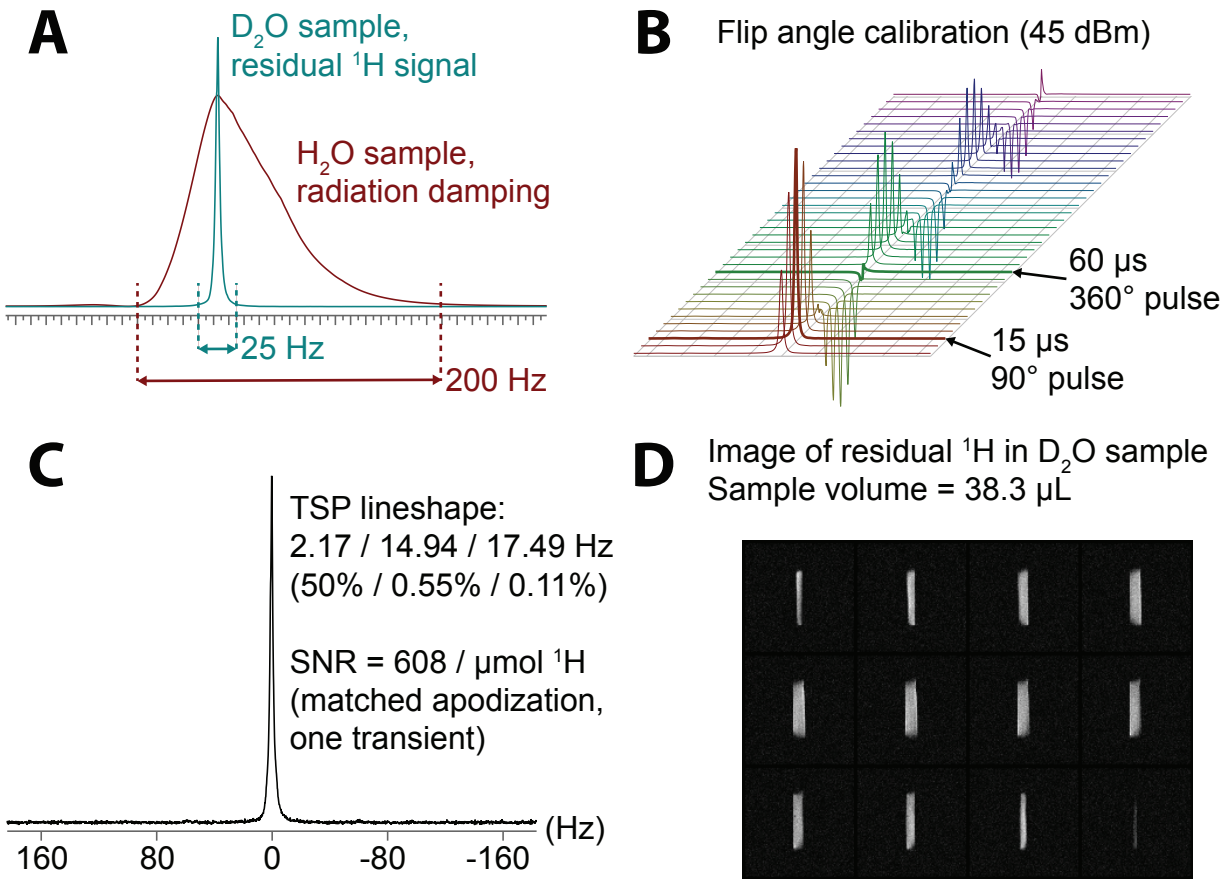

Figure 1.6. Performance characterization of RF microcoil. A. Observation of radiation damping effect with a pure H_2O sample necessitated switching to a D_2O sample. B. 90° flip angle calibration was 15 µs at 45 dBm. C. TSP lineshape was 2.17 / 14.94 / 17.49 Hz (one transient, no apodization) and SNR was 608 per µmol ^1H (one transient, matched apodization). D. Sample volume visible to the coil was 38.3 µL, measured using a 2D multislice interleaved gradient echo sequence with a 20 mm × 20 mm field of view and 128 × 128 matrix with 200 µm thick slices (TR = 300 ms, TE = 4 ms, 20° flip angle, and 10 averages). The image depicted was acquired from residual ^1H within the D_2O / 0.05 % TSP sample.

Discussion

In this study, we constructed a 600 MHz microcoil suitable for micro-imaging of small samples such as individual prostate biopsies. The mass-adjusted SNR achieved by the present room-temperature 2.2 mm inner diameter RF microcoil was 608 / µmol ^1H. This was similar to a reported sensitivity of 651 / µmol ^1H for a 5 mm inner diameter

600 MHz cryoprobe[38] with higher-order shims, and superior to the 220 / μmol ^{1}H reported for a room-temperature 5 mm 600 MHz probe,[38] suggesting that the achieved sensitivity was competitive with commercially available NMR probes.

The careful choice of materials used for the RF coil fabrication were critical to the sensitivity performance that we achieved. However, the achievable RF coil sensitivity was limited by the shimming capabilities of the 14.1 T MRI scanner, which yielded a TSP 50% linewidth of 2.17 Hz as compared to < 1 Hz on high-resolution spectrometers. To achieve even higher sensitivity it would be necessary to build or install higher-order shims, or adapt the coil for use with a different spectrometer. However, it should be noticed that our 14.1 T MRI system lacked higher-order shims due to the installation of high-power imaging gradients up to 1 T / m (100 gauss / cm), which were ideally suited for the micro-imaging purpose for which we originally designed the RF microcoil.

Acknowledgements

We are grateful for critical input on RF coil engineering from Lucas Carvajal of UCSF, Anita Flynn of UC Berkeley, Mark VanCriekinge of UCSF, and Professor Steven Conolly of UC Berkeley. Professor Shuvo Roy's lab at UCSF provided access to the ANSYS software, soldering tools and a network analyzer. The Center for Advanced Technology at UCSF provided access to the Othermill router and uPrint 3D-printer.

Chapter 2. Micro-DWI of Single Prostate Biopsies at 14 T with 50 μm Resolution

Introduction

Magnetic resonance (MR) diffusion-weighted imaging (DWI) is among the most useful prostate imaging techniques in current clinical practice.[39,40,41,42] DWI is sensitive to the motion of water molecules at microscopic spatial scales within biological tissues, and the apparent diffusion coefficient (ADC) of water can provide unique information about microscopic tissue compartments, and the pathology of prostate tissues.[43] In patients, the ADC has been shown to be lower in prostate cancer than in surrounding benign prostate tissues, with typical ADC values ranging from 2.0×10^{-3} mm^2/s to 1.4×10^{-3} mm^2/s for benign tissues and 1.6×10^{-3} mm^2/s to 0.8×10^{-3} mm^2/s for cancer, respectively.[44,45] MR diffusion has also shown promise for reflecting the pathologic grade of prostate cancer, with lower ADC values found in higher Gleason score cancers. In a 2012 study, ADC decreased from $1.135 \pm 0.119 \times 10^{-3}$ mm^2/s in patients with Gleason 6(3+3), to $0.976 \pm 0.103 \times 10^{-3}$ mm^2/s in patients with Gleason 7(3+4), to $0.831 \pm 0.087 \times 10^{-3}$ mm^2/s in patients with Gleason 7(4+3) prostate cancer.[46]

In ex vivo experiments of human prostate biopsies, metabolic measurements such as high resolution magic angle spinning (HR-MAS) and/or hyperpolarized ^{13}C (HP ^{13}C) data are confounded by the large amount of tissue heterogeneity, both benign and malignant tissues, in a single prostate biopsy sample. Specifically, varying amounts of cancer and the presence of cancers of varying pathologic grade in a single biopsy core confuses the interpretation of cellular metabolic changes associated with prostate cancer presence and pathologic grade from whole biopsy metabolic measurements.

Micro-DWI measurements of prostate biopsies could provide a means of assessing the amount and pathologic grade of cancer present and thereby improve the assessment of the metabolic changes associated with cancer aggressiveness as well as with therapeutic response. Consequently, using the custom-engineered 600 MHz RF microcoil described in Chapter 1, we endeavored to obtain water ADC images from individual prostate biopsies using ex vivo micro-DWI at 14 tesla.

There have been numerous prior studies of prostate DWI both in vivo[19,39,40,41,42] and ex vivo,[47] and micro-DWI of formalin-fixed prostate tissue has been previously performed with 40 μm resolution.[48,49] To our knowledge, micro-DWI of freshly acquired unfixed prostate biopsies has not been previously performed.

Theory

Brownian motion. Molecules in solution undergo Brownian motion due to thermal kinetic energy.[50,51] The particle displacement of Brownian motion follows a Gaussian distribution, with mean squared displacement given by $2D\Delta$, with D being the diffusion coefficient, typically measured in mm^2/s, and Δ (in s) being the measurement timescale.[50,51]

Diffusion-weighted imaging. Conventional spin-echo diffusion-weighted imaging uses gradients to impose a spatially dependent phase on the magnetization, which is then reversed using a 180° pulse and additional gradients.[52,53] The magnetization of static spins remains coherent during readout, whereas the apparent signal of diffusing spins is reduced due to phase decoherence. Assuming the so-called "mono-exponential" model of diffusion-weighted signal decay, the expected signal amplitude for

spins with a given diffusion coefficient *D* may be computed using modified Bloch equations.[52,53]

$$\frac{S}{S_0} = e^{-\frac{\mathrm{TE}}{T_2}} e^{-bD} \qquad (2.1)$$

$$b = -\gamma^2 G^2 \delta^2 \left(\Delta - \frac{\delta}{3}\right) \qquad (2.2)$$

In Eq. (2.1) and (2.2), *D* is termed the apparent diffusion coefficient (ADC). The diffusion-weighting parameter *b* in s/mm^2 describes the degree of signal decay imposed by the amplitude *G*, duration *δ*, and spacing Δ of the diffusion gradients and is also sensitive to the gyromagnetic ratio *γ*, which determines the rate of phase accumulation under the influence of gradient amplitude *G*. The diffusion time parameter Δ is also important because for a given *D*, the majority of particles will only travel a displacement sqrt(2*D*Δ), meaning that the imaging sequence will not be sensitive to diffusion barriers greater than this characteristic distance.

Tissue cellularity. The cytosol has a high density of organelles and proteins that impede the diffusion of water. Consequently, the cytosolic diffusion coefficient of water is lower, by up to an order of magnitude, than the diffusion coefficient in the comparatively dilute extracellular fluid.[51,54] High tissue cellularity, as seen in prostate tumors, is therefore visible as restricted diffusion (decreased ADC) on DWI.[19,39,40,41,42]

Tissue microarchitecture. Histologically, the normal prostate consists of branching ducts surrounded by layers of epithelial cells, embedded within a stromal background.[55] The diffusion coefficient of water is expected to be highest in the ductal lumen and lowest within cells, with an intermediate diffusion coefficient for the extracellular space. Clinical DWI fitted using a mono-exponential diffusion signal decay

model would therefore be expected to volume-average these different tissue compartments within a single voxel, and the reported ADC value would be related to the relative proportions of the different tissue compartments at a given location. Thus, increased cellularity and/or decreased luminal space are believed to be responsible for the diffusion restriction that is clinically observed in prostate tumors.[48,49]

Perfusion. In vivo there is a fast perfusion component to the water ADC whereas in the ex vivo setting this is not the case. However at *b*-values above approximately 180 s/mm^2 the perfusion component is thought to be fully suppressed during in vivo imaging, and is therefore invisible to the ADC calculation.[56]

Cellular swelling. In human tissue, physiologic water and osmotic balance across cellular membranes is established primarily by the action of the Na^+ / K^+ ATPase. Under hypoxia due to ischemia, within a few minutes of onset there is a decrease in ATP levels and homeostatic function of the Na^+ / K^+ ATPase. This, in turn, causes an osmotic shift of extracellular water into the cytosol, which decreases the ADC.[54] Therefore, fresh ex vivo tissue with intact cellular membranes would be expected to display reduced ADC as compared to the in vivo setting. This effect would be unavoidable due to the rapid onset of cellular swelling following ischemia. However, it is unclear whether the effect might further increase over time.

Ischemia and apoptosis. There is evidence of an ischemic gene expression signature within one hour of harvesting prostate tissue from patients.[57] However, it is unclear how quickly the cellular membranes will bleb and rupture from apoptosis and/or necrosis, which will eventually increase the ADC as compared to the in vivo setting (in contrast to early cellular swelling, which decreases the ADC). In this study, the biopsy

tissues experienced less than 1.5 hours of cold ischemia after acquisition, followed by 2.5 hours of warm ischemia during shimming and imaging. The formalin-fixed biopsy sections obtained from this protocol demonstrated intact tissue morphology.

Temperature. The ADC is proportional to absolute temperature,[50] meaning that ex vivo DWI acquired at room temperature would be expected to have a lower ADC compared to the in vivo scenario. However, this effect is small, given that the ratio of ex vivo to in vivo absolute temperature is 293.15 K / 310.15 K = 0.945.

Tissue fixation. There are many published reports of ex vivo DWI of fixed tissues,[48,49] which were treated with an agent such as 10% neutral buffered formalin which is believed to crosslink proteins and cell membranes without causing cellular swelling. There is evidence to suggest that the fixation process reduces the ADC compared to in vivo, potentially due to crosslinking creating additional barriers to water diffusion.[58]

Materials and Methods

Biopsy acquisition. Transrectal 18-gauge prostate biopsies from patients undergoing active surveillance for prostate cancer were acquired with Institutional Review Board approval. Biopsies were acquired using an ultrasound-MRI fusion system that provided registration of transrectal ultrasound images to prior prostate MRI (UroNav, InVivo, Inc.). Up to two research biopsies per patient were acquired from any visible MRI or ultrasound lesions once the clinical biopsy acquisition had been completed. Biopsies were stored in phosphate-buffered saline on ice for up to 1.5 hours prior to imaging. The median storage time was 0.5 hours.

Sample preparation. Biopsies were removed from phosphate-buffered saline and loaded into a hemisected 2.2 mm diameter Kapton catheter (MicroLumen, Inc.). Biopsy cores greater than 9 mm in length were folded over to fit within the sensitive region of the 2.2 mm diameter × 9 mm length RF microcoil. A small drop of cyanoacrylate adhesive was used to attach the biopsy sample to the catheter at either end of the sensitive region. The hemisected catheter was loaded into the RF microcoil sample chamber, which was then filled with Fluorinert FC-40 (Sigma-Aldrich, Inc.) susceptibility matching fluid. We found that this ^{1}H MRI-invisible fluid mostly eliminated air bubbles from the sample chamber due to its extremely low polarity and surface tension.

MRI preparation. The micro-DWI data was acquired within a Varian 600 MHz (14.1 tesla) small animal MRI system. Due to the high sensitivity of the RF microcoil to dielectric sample loading, the microcoil was tuned and matched for each sample using a benchtop network analyzer, with fine adjustments made inside of the MRI scanner. The 90° RF pulse was calibrated for each sample. Each biopsy sample was positioned at isocenter of the MRI scanner using scout sequences and was 3D gradient-shimmed.

Micro-DWI pulse sequence. 3D spin-echo micro-DWI images were acquired using TR = 700 ms, TE = 38.97 ms, 12.8 mm × 3.2 mm × 1.2 mm field of view, 256 × 64 × 24 matrix, and readout bandwidth = 12.5 kHz, yielding 50 μm isotropic resolution. The diffusion gradients had duration δ = 2 ms with spacing Δ = 12 ms. There were six diffusion directions acquired at b = 600 s/mm^2 in addition to the b = 0 s/mm^2 acquisition, yielding a total imaging time of 2 hours and 6 minutes.

Trace ADC calculation. We used the mono-exponential signal decay model of diffusion-weighted imaging data. In this model,

$$\mathbf{s} = -\mathbf{B}\mathbf{d} \qquad (2.3)$$

Where **s** is a vector of logarithms of signal values, **B** is a matrix of diffusion-weighting *b*-values, and **d** is a vector of diffusion coefficients. Eq. (2.3) becomes clearer when written out in component-wise form:

$$\begin{pmatrix} \ln(S_1) \\ \ln(S_2) \\ \ln(S_3) \\ \ln(S_4) \\ \ln(S_5) \\ \ln(S_6) \\ \ln(S_7) \end{pmatrix} = - \begin{pmatrix} b_{1\mathrm{ss}} & b_{1\mathrm{sp}} & b_{1\mathrm{rs}} & b_{1\mathrm{pp}} & b_{1\mathrm{rp}} & b_{1\mathrm{rr}} & 1 \\ b_{2\mathrm{ss}} & b_{2\mathrm{sp}} & b_{2\mathrm{rs}} & b_{2\mathrm{pp}} & b_{2\mathrm{rp}} & b_{2\mathrm{rr}} & 1 \\ b_{3\mathrm{ss}} & b_{3\mathrm{sp}} & b_{3\mathrm{rs}} & b_{3\mathrm{pp}} & b_{3\mathrm{rp}} & b_{3\mathrm{rr}} & 1 \\ b_{4\mathrm{ss}} & b_{4\mathrm{sp}} & b_{4\mathrm{rs}} & b_{4\mathrm{pp}} & b_{4\mathrm{rp}} & b_{4\mathrm{rr}} & 1 \\ b_{5\mathrm{ss}} & b_{5\mathrm{sp}} & b_{5\mathrm{rs}} & b_{5\mathrm{pp}} & b_{\mathrm{rp}} & b_{5\mathrm{rr}} & 1 \\ b_{6\mathrm{ss}} & b_{6\mathrm{sp}} & b_{6\mathrm{rs}} & b_{6\mathrm{pp}} & b_{6\mathrm{rp}} & b_{6\mathrm{rr}} & 1 \\ b_{7\mathrm{ss}} & b_{7\mathrm{sp}} & b_{7\mathrm{rs}} & b_{7\mathrm{pp}} & b_{7\mathrm{rp}} & b_{7\mathrm{rr}} & 1 \end{pmatrix} \begin{pmatrix} D_{\mathrm{ss}} \\ D_{\mathrm{sp}} \\ D_{\mathrm{rs}} \\ D_{\mathrm{pp}} \\ D_{\mathrm{rp}} \\ D_{\mathrm{rr}} \\ \ln(S_0) \end{pmatrix} \qquad (2.4)$$

In this equation, the indices 1 … 7 correspond to *b*-value directions (six directions plus one non-diffusion weighted acquisition), while the subscripts ss, sp, etc. describe components in imaging coordinates (“s” corresponds to “slice-select”, “p” corresponds to “phase-encode,” and “r” corresponds to “readout”). The matrix **B** was computed by the 3D spin echo with diffusion pulse sequence program in VNMRJ 4. The analysis problem was to invert this **B** matrix to obtain the diffusion coefficient vector **d** in terms of the logarithm-of-signal vector **s**. The matrix **B** was inverted numerically using QR decomposition in MatLab (The MathWorks, Inc.). The first six components of the resulting diffusion coefficient vector **d** were formulated as the diffusion tensor **D**:

$$\mathbf{D} = \begin{pmatrix} D_{\mathrm{ss}} & D_{\mathrm{sp}} & D_{\mathrm{rs}} \\ D_{\mathrm{sp}} & D_{\mathrm{pp}} & D_{\mathrm{rp}} \\ D_{\mathrm{rs}} & D_{\mathrm{rp}} & D_{\mathrm{rr}} \end{pmatrix} \qquad (2.5)$$

The eigenvalues λ_1, λ_2, and λ_3 of **D** were computed, and were used to compute the trace apparent diffusion coefficient (ADC) value for each voxel within the image, yielding a trace ADC image:

$$\text{ADC}_{\text{trace}} = \frac{\lambda_1 + \lambda_2 + \lambda_2}{3} \quad (2.6)$$

Further, a synthetic diffusion-weighted image was computed using the maximum *b*-value that was applied (i.e., the largest element of matrix **B**) and the trace ADC value at each voxel. It should be noted that because true "b=0 s/mm^2" images are not achievable in a real imaging system, the parameter S_0 is in fact a synthetic value obtained from inversion of **B** in Eq. (2.4).

$$S_{\text{dw, synthetic}} = S_0 e^{-b_{\text{max}}\text{ADC}_{\text{trace}}} \quad (2.7)$$

Micro-DWI data analysis. We found that although the biopsy samples were submerged in Fluorinert FC-40, it was nevertheless necessary to segment the biopsy samples from surrounding phosphate-buffered saline. A signal threshold on "*b*=0" s/mm^2 images was used to generate an initial binary mask that excluded regions containing Fluorinert FC-40 and/or noise. Next, voxels with trace ADC > 2.0 × 10^{-3} mm^2/s were excluded under the assumption that these voxels corresponded to phosphate-buffered saline. Finally, the mask was blurred using a 3 × 3 × 3 kernel and was re-binarized, which we found was sufficient to fill any mask holes attributable to imaging noise, while preserving holes that were attributable to an absence of tissue at a given location. This segmentation procedure was implemented as an automated algorithm in MatLab. Finally, the trace ADC histograms for each biopsy sample were plotted, and the mean and 10$^{\text{th}}$ percentile ADC values were computed.

Comparison to in vivo DWI. The clinical DWI sequence at our institution used an oblique axial slice plan with a 24 cm field of view, 256 × 128 matrix, 4 mm thick slices, and TE = 52.9 ms. The sequence used parallel imaging with an acceleration factor of 2

and an echoplanar acquisition scheme.[59] The diffusion parameters were b = 0 and 600 s/mm^2, Δ = 22.1 ms, and δ = 7.3 ms with six diffusion gradient directions acquired. The mean trace ADC values corresponding to the MRI lesion were extracted from the clinical radiology reports within the picture archiving and communications system (PACS) at our institution. We computed the percentage change of the ADC between ex vivo and in vivo samples, $100*(ADC_{\text{ex vivo}} - ADC_{\text{in vivo}}) / ADC_{\text{in vivo}}$.

Biopsy histopathology. Following imaging, the biopsy samples were fixed in 10% neutral-buffered formalin, embedded in paraffin, sectioned, and stained with hematoxylin and eosin (H&E) and high-molecular weight cytokeratin for interpretation by a board-certified genitourinary pathologist. For each sample the pathologist determined the primary Gleason pattern, secondary Gleason pattern, Gleason score, percentage of cancer, percentage of glandular tissue, and percentage of stromal tissue.

Results

Biopsy dataset. We collected n=5 fresh biopsy samples from five different patients, which included three PI-RADS (Prostate Imaging Reporting and Data System) 3 samples and two PI-RADS 4 samples. Of these samples, all five were benign, with the percentage of glandular tissue ranging from 10% to 50%. Two of the research samples originated from MRI lesions that produced at least one clinical cancer biopsy, most likely due to sampling differences during repeat biopsies of the same lesion.

Example case. In Figure 2.1A, clinical T_2-weighted, DWI and trace ADC images demonstrate a PI-RADS 4 lesion in the right lateral peripheral zone at the level of the midgland (trace ADC = 1.08×10^{-3} mm^2/s). In Figure 2.1B, we see ex vivo DWI of the

biopsy sample acquired from the MRI lesion. Images have been masked to display only biopsy voxels. In Figure 2.1C, we see the ex vivo trace ADC image of the biopsy sample acquired from the MRI lesion. In Figure 2.1D, we see the H&E stain. The biopsy sample consisted of 40% glandular tissue as determined by a board-certified genitourinary pathologist.

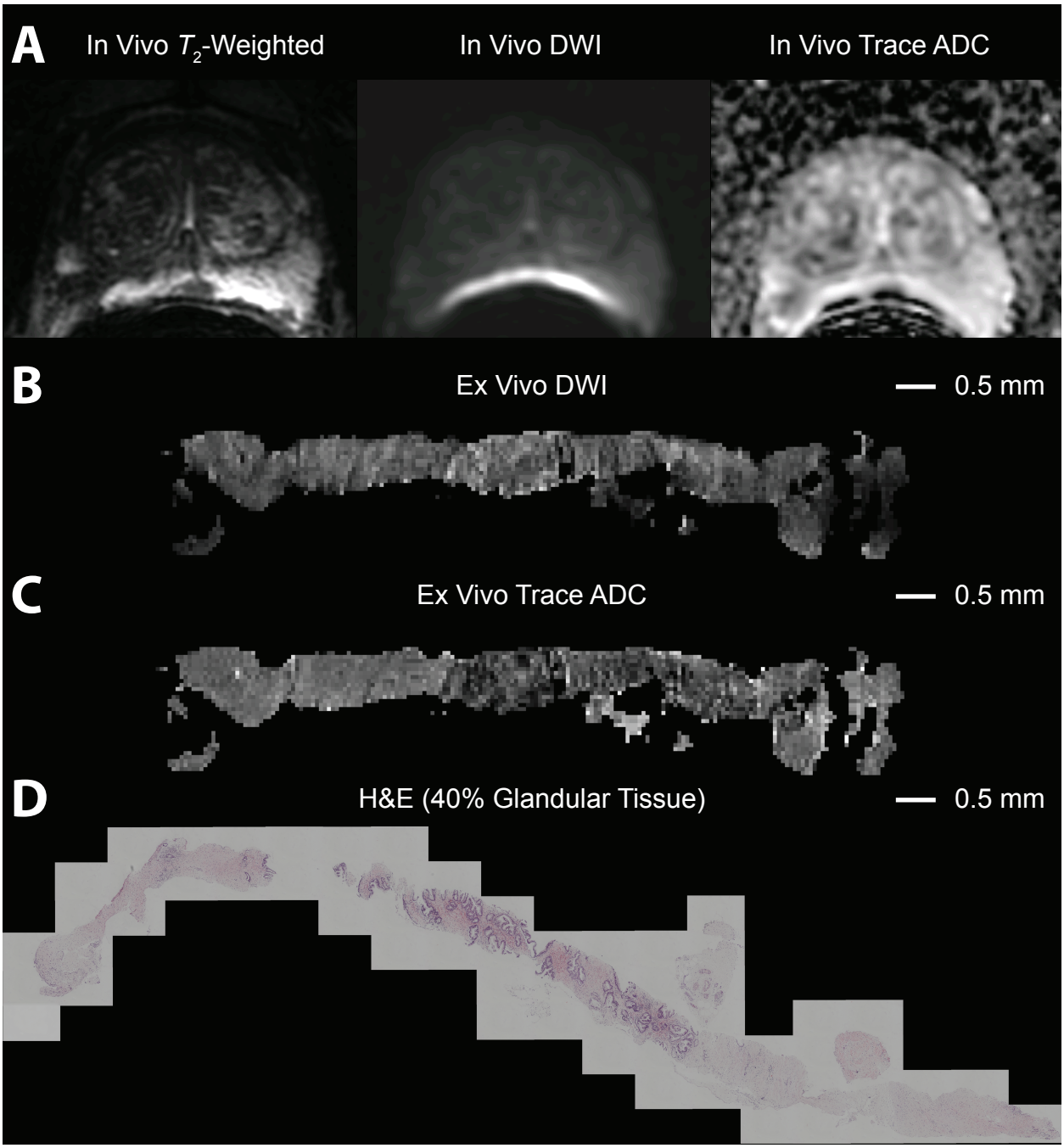

Figure 2.1. Example ex vivo micro-DWI case.

Biopsy ADC histograms. We observed approximately Gaussian biopsy ADC histograms with modal ADC values close to 1.0×10^{-3} mm^2/s (Figure 2.2). One of the 10% glandular biopsy samples had a positively skewed ADC histogram, whereas the 40% and 50% glandular biopsy samples had negatively skewed ADC histograms. We

observed a negative Spearman rank correlation ($p < 0.05$) between the biopsy glandularity and the 10th percentile ADC value, highlighted in red in Figure 2.2A. In Figure 2.2B, we see the corresponding micro-DWI images from each sample, taken as representative sections from the 256 × 64 × 24 matrix size 3D images. All DWI images are displayed with the same window/level settings to facilitate visual comparisons. In Figure 2.2C, we see the percentage of benign glandular tissue assigned by a board-certified genitourinary pathologist viewing H&E stained specimens.

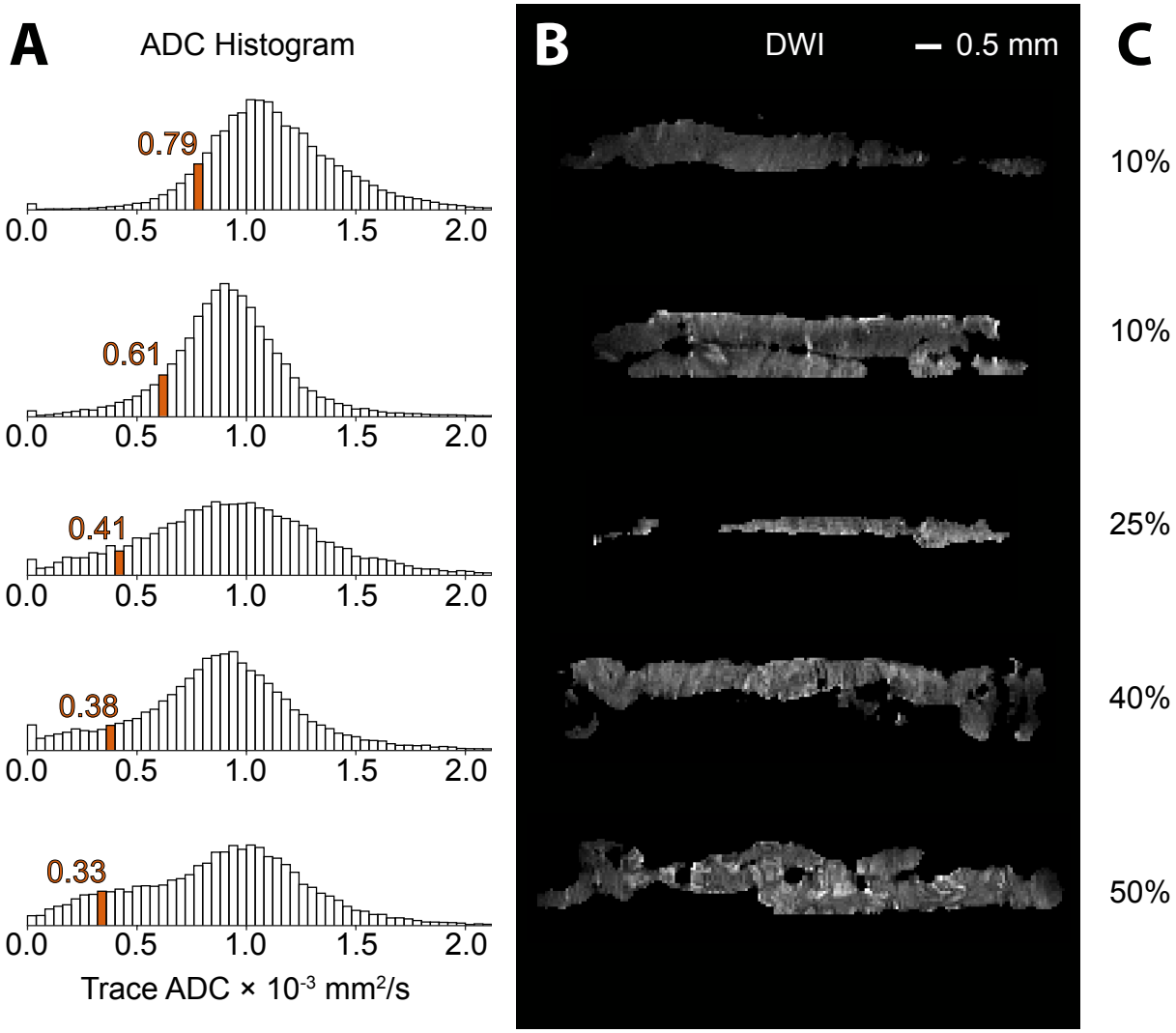

Figure 2.2. Results from ex vivo micro-DWI of prostate biopsy samples.

Comparison to in vivo ADC values. The mean trace ADC values of the biopsies at micro-DWI were typically lower than the mean in vivo ADC values of the MRI lesions by 17% to 27% (Figure 2.3). In one case, the ex vivo ADC value was 46% higher; however, the clinical biopsy from that lesion was Gleason 3+4 cancer whereas the research biopsy sample was benign, most likely reflecting differences in sampling of the lesion.

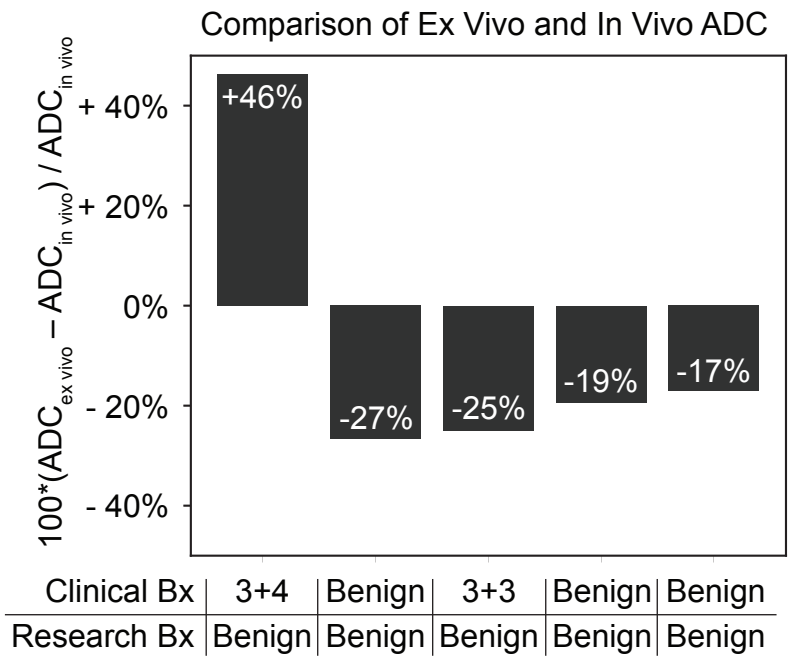

Figure 2.3. Comparison of ex vivo and in vivo ADC values. Positive values indicate that the ex vivo ADC was higher. The comparison of pathology interpretations for the research biopsy (Research Bx) vs. the clinical biopsy (Clinical Bx) is enumerated.

Discussion

In this study, we acquired micro-DWI of freshly acquired unfixed prostate biopsies using a custom-engineered 600 MHz RF microcoil. Furthermore, we observed lower 10th percentile ADC values in benign samples of higher cellularity, which gave qualitative agreement with the report of Bourne et al. in which a higher *b*-value of 1200 s/mm^2 was used.[48] We observed generally lower ex vivo ADC values in comparison to in vivo values, an observation compatible with cellular swelling due to biopsy ischemia as well as lower temperatures in the ex vivo setting.

This study had a number of limitations. The ex vivo diffusion time of Δ = 12 ms limited the mean squared displacement for a single particle to under 5 μm for a particle experiencing an apparent diffusion coefficient of 1.0×10^{-3} mm^2/s. This might have limited the range of ADC values that could be sampled, as compared to the clinically employed diffusion time of Δ = 22.1 ms at our institution. In our view, the decision to scan fresh unfixed prostate biopsies was more biologically realistic than scanning formalin-fixed samples, but we were not able to directly assess the impact that cellular swelling due to ischemia might have had upon our results. Finally, the biggest limitation of the study was the fact that all of the biopsy samples studied to date were benign.

Future studies involving the acquisition of a significant number of cancer biopsies of varying pathologic grade, and quantitative correlation of ADC images with histopathology, will be necessary to validate the micro-DWI technique in providing an accurate means of assessing the percentage and pathologic grade of prostate cancer in individual biopsy samples.

Acknowledgements

We wish to thank Professor Susan Noworolski for feedback on DWI acquisition parameters and the interpretation of diffusion-weighted imaging data. We are grateful to Jeremy Gordon and Professor Peder Larson of UCSF for useful discussions on the choice of acquisition parameters for diffusion-weighted imaging. Subramaniam Sukumar provided essential technical assistance with the use of the 14.1 T small animal MRI scanner. Romelyn Delos Santos prepared the histology specimens, and Laura Tabatabai interpreted the biopsy samples. Dr. Katuso Shinohara and Dr. Hao Nguyen of

the UCSF Department of Urology acquired the research biopsy samples for this study. Dr. Antonio Westphalen of the UCSF Department of Radiology provided essential assistance for accessing the clinically outlined prostate MRI lesions using the DynaCAD software. Finally, we wish to thank the patients who provided their tissue for this study.

Chapter 3. NMR Quantification of Lactate Production and Efflux and Glutamate Fractional Enrichment in Living Human Prostate Biopsies Cultured with [1,6-$^{13}C_2$]Glucose

Introduction

Prostate cancer metabolism is characterized by a shift to aerobic glycolysis and lactate production, known as the Warburg effect.[7,8,9,10,11] Yet, it is not currently known how tumor metabolism changes in the setting of human castration-resistant and/or neuroendocrine prostate cancer (CRPC/NEPC). Recent studies have identified genetic alterations with significant putative metabolic effects in human CRPC.[20,21] To investigate these effects, it is essential to measure metabolism in living human prostate tissue. Our laboratory has previously employed an optimized rotary tissue culture system to perform ^{13}C NMR metabolic labeling studies in slices of human prostate tissue acquired from radical prostatectomy (RP).[17,60,61] Yet, RP is not standard of care for CRPC or NEPC, so the tissue slice technique cannot be applied in this clinically significant cohort of patients to yield a better insight into their respective metabolic adaptations. While it is clinically feasible to obtain biopsy samples from patients with CRPC and/or NEPC, a novel metabolic profiling protocol that is optimized for living human biopsies is needed to study these specimens.

In the current work, we demonstrate that the combination of rotary biopsy culture, ^{13}C metabolic labeling, and NMR can quantify metabolism in freshly acquired living human prostate biopsies. The current research focuses on the development of the techniques necessary to acquire and measure the Warburg effect in living patient-derived biopsies, acquired from patients prior to treatment for the determination of cancer presence, Gleason grade and extent for personalized therapeutic selection. By

definition this was an early stage cancer patient population, resulting in the acquisition of mainly benign and low grade (primary Gleason pattern 3) prostate cancer biopsies in this study. However, the ultimate goal is to utilize the optimized techniques developed in this study to assess the Warburg effect and other changes in metabolism in patients with advanced disease who would not normally receive surgical therapy.

A particular motivation for studying the metabolism of prostate cancer comes from the preclinical and clinical development of hyperpolarized ^{13}C MRI techniques,[13,14,15,16] with clinical trials of hyperpolarized [1-^{13}C]pyruvate in prostate cancer now underway at multiple sites.[62] In prostate cancer, there is considerable heterogeneity of prognosis for prostate cancer patients, particularly for patients with a ≤ Gleason 7 histopathological score.[4] Therefore, there is significant potential for hyperpolarized ^{13}C metabolic imaging of primary prostate cancer to provide additional information to the clinician, in combination with Gleason scoring and clinical risk scores such as the Cancer of the Prostate Risk Assessment (CAPRA) score.[5] In the metastatic setting, it is widely recognized that metabolic responses to therapy can significantly precede anatomical responses,[63] which means that hyperpolarized ^{13}C metabolic imaging may be able to better inform in real-time spatially resolved treatment monitoring for the clinician and patient in conjunction with serum tumor markers such as the prostate-specific antigen (PSA).[6]

In hyperpolarized ^{13}C MRI, the measured signal is proportional to the product of (a) probe polarization, (b) the fractional enrichment of the precursor being converted to the produced metabolite, and (c) the pool size of the produced metabolite.[64] In the *ex vivo* setting it becomes possible to disentangle these factors, ideally leading to a better

interpretation and understanding of the hyperpolarized ^{13}C signal,[17] and enabling the development of new hyperpolarized probes and potential therapeutic targets.

A significant challenge in the metabolic profiling of specific biochemical pathways using stable isotopes in individual living prostate biopsies by NMR is the small tissue mass ranging from 1 mg to 6 mg, which limits the achievable signal-to-noise ratio (SNR). Therefore, in the present work we have focused on optimizing the experimental parameters such as the duration of time in rotary biopsy culture and the parameters of the NMR acquisition so as to achieve sufficient metabolite signals from a small mass of tissue incubated with ^{13}C labeled metabolic substrates.

Methods

Biopsy acquisition. Transrectal 18-gauge prostate biopsies from 22 previously untreated patients (34 total biopsies, 27 normal prostate biopsies, five Gleason 6(3+3) cancer biopsies, and two Gleason 7(3+4) cancer biopsies) were acquired with Institutional Review Board approval. Biopsies were acquired using an ultrasound-MRI fusion system that provided registration of transrectal ultrasound images to prior prostate MRI (UroNav, InVivo, Inc.). Up to two research biopsies per patient were acquired from any visible multiparametric ^{1}H MRI or ultrasound lesions once the clinical biopsy acquisition had been completed. In cases with fewer than two visible lesions, a biopsy was sometimes taken from a normal-appearing area of the peripheral zone. Immediately following acquisition, biopsies were stored in vials on ice and were transferred to rotary culture within 15 minutes.

Biopsy culture medium. A formulation of PFMR-4A medium with supplements optimized for prostate tissue culture was previously described.[60,61] For this study, it was found that HEPES and threonine in this medium posed a potential challenge for the quantification of NMR spectra. Consequently, we developed a formulation of bicarbonate-buffered, HEPES-free, threonine-free, pyruvate-free F-12 medium containing all of the previously described supplements.[60,61] (The complete medium recipe is provided in Supporting Information.) For labeling studies, the medium contained exclusively [1,6-$^{13}C_2$]glucose at 1.0 g/L.

Biopsy rotary tissue culture. Techniques previously described for the culture of thin, precision-cut prostate tissue slices[60] were adapted for culture of biopsies. Each biopsy was loaded onto a titanium mesh inside of one well of a 6-well plate containing 2.5 mL per well of pre-warmed F-12 prostate medium with [1,6-$^{13}C_2$]glucose. The plates were loaded onto a rotary tissue culture system (Alabama R&D, Inc., Figure 3.1B) within a 37 °C, 5% CO_2 incubator, and the biopsies were cultured for either 24 or 26 hours. For a subset of samples, the biopsy culture medium was collected and replaced with fresh pre-warmed medium at the 2 hour timepoint in order to quantify the initial rate of lactate efflux, in addition to the lactate efflux after 24 hours of culture. Each 6-well plate also contained a control well containing medium but without any biopsy tissue. At the end of the culture period, the medium was collected and stored at –80 °C.

Biopsy rinsing. After culture the biopsies were placed in ice-cold phosphate-buffered saline for less than one minute, blotted with a delicate task wipe and stored at –80 °C. This procedure was intended to remove medium that could otherwise

contaminate the post-culture biopsy High Resolution-Magic Angle Spinning (HR-MAS) NMR spectra as we have shown previously.[65]

Biopsy tissue NMR measurements. Frozen biopsies were loaded without thawing into a sealed zirconium HR-MAS rotor[65,66] on a tared digital balance to measure the wet weight of the biopsy tissue. Six µL of D_2O/0.05% trimethylsilylpropanoic acid (TSP) solution was further added to the rotor and weighed to enable deuterium locking as well as a chemical shift reference via TSP. The HR-MAS rotor was sealed and loaded into a 500 MHz Varian gHX Nano (proton-carbon double resonance) 4 mm indirect detection HR-MAS probe maintained at 1 °C. Acquisition was performed at a spin rate of 2.25 kHz using a Varian Inova console with VNMRJ 4 after locking on the D_2O signal. The probe tuning, 90° pulse width and water saturation frequency were calibrated for each sample. Each sample was shimmed using an automated FID shimming routine for 20 minutes (see Supporting Information). ^{1}H Carr-Purcell-Meiboom-Gill (CPMG) spectra were acquired with 60,000 complex points, 3 second acquisition time, 2 second water suppression pulse, 6 second overall repetition time, and 1,024 scans. It was previously established that this repetition time yielded fully relaxed spectra in human prostate tissue.[35] The CPMG echo time was set to 288 ms. The spacings of 180° pulses within the CPMG sequence were synchronized to the spinning period of the rotor.[35] To quantify metabolite total pools in addition to ^{13}C labeled fractions, CPMG datasets were acquired both with and without heteronuclear ^{13}C decoupling using a GARP pulse[65,67] for a total CPMG scan time of 3 hours, 25 minutes.

Biopsy histopathology. Following the HR-MAS data acquisition, the biopsies were fixed in 10% neutral-buffered formalin, embedded in paraffin, sectioned, and stained

with hematoxylin and eosin (H&E) and high-molecular weight cytokeratin for interpretation by a board-certified genitourinary pathologist. For each sample the pathologist determined the primary Gleason pattern, secondary Gleason pattern, Gleason score, percentage of cancer, percentage of glandular tissue, and percentage of stromal tissue.

Biopsy media NMR measurements. The samples of biopsy medium were thawed from storage at –80 °C. NMR samples were prepared by adding 65 mg of D_2O/0.05% TSP to 540 mg of conditioned medium and placed in 5 mm NMR tubes. The sample data were acquired at 600 MHz using a Bruker Avance III console equipped with a 5 mm Bruker BBFO (broadband double resonance) direct detection probe. The 90° pulse was calibrated, and automated z-axis shimming was performed up to 8^{th} order in addition to tuning of all first-order shims (see Supporting Information). Water-suppressed data were acquired using a fully relaxed ZGCPPR pulse sequence with a 12 s acquisition time (114,942 points) and 3 s relaxation delay and 32 scans (8 minutes per sample).

NMR data processing. All NMR datasets were processed in MestreNova 12 (Mestrelab Research S.L.). The datasets were zero-padded by a factor of 2, apodized with a 0.25 Hz exponential filter and automatically phased and baselined using a Whittaker smoother algorithm[68] and manually adjusted as needed. Peaks of interest were automatically picked and fitted using a Lorentzian-Gaussian shape function with a simulated annealing algorithm (500 coarse iterations, 100 fine iterations, and a local minima filter of 25 were used). All automated peak fits were tweaked after visual assessment for fit quality based on the residual signal and adjusted when necessary.

NMR quantification. In the biopsy HR-MAS CPMG data, peak areas were quantified relative to the calibrated amplitude of the Electronic REference To access In vivo Concentrations (ERETIC) signal, corrected for the number of metabolite protons.[66] Appropriate T_2 corrections were applied based upon HR-MAS measurements in human prostate tissue at 1 °C and 500 MHz (lactate C3 T_2 = 251 ms, glutamate C4 T_2 = 275 ms).[10,17] Metabolite amounts were further standardized by the wet tissue weight of the sample, to yield a biopsy metabolite concentration in (nmol/mg). Fractional enrichments were computed as follows.

$$FE_{Lac,\ C3} = \frac{\left[3\text{-}^{13}C\ Lac\right]\Big|_{cpmg}}{[Total\ C3\ Lac]|_{hetnuc\ decoupled\ cpmg}} \qquad (3.1)$$

$$FE_{Glu,\ C4} = \frac{[Total\ C4\ Glu]|_{hetnuc\ decoupled\ cpmg} - \left[4\text{-}^{12}C\ Glu\right]\Big|_{cpmg}}{[Total\ C4\ Glu]|_{hetnuc\ decoupled\ cpmg}} \qquad (3.2)$$

The glutamate fractional enrichment at the 4-position was computed by differencing the quantification of the 2.34 ppm C4 multiplet in the ^{13}C decoupled vs. non-decoupled CPMG spectrum. This obviated the need to quantify the [4-^{13}C]glutamate satellite peaks, which are known to underlie other peaks such as the [4-^{12}C]glutamine peak and additionally could be further split by the presence of [3-^{13}C]glutamate labeling on the same molecule (Figure 3.1D, Figure 3.5).

In the fully relaxed media data, the lactate peak area was quantified relative to the known peak area and measured mass of TSP, and corrected for the relative number of protons. The lactate amount was further standardized by the wet tissue weight of the biopsy, as well as the duration of the biopsy tissue culture, to yield a lactate efflux rate in (nmol/min)/(mg tissue).

LIVE/DEAD assays and imaging. At the end of the culture experiment, a limited number of biopsies were transferred to a new well containing medium with ethidium homodimer-1 at 0.5 μmol/L and calcein-AM at 2.5 μmol/L.[69] The biopsies were maintained in culture for a further two hours and then rinsed for 10 minutes in phosphate-buffered saline under dark conditions before blotting with a delicate task wipe and imaging on a laser scanning confocal microscope (Zeiss 780). A two-photon excitation was used at a 759 nm wavelength with a 25× water immersion objective, a 1024 by 1024 image size, and 2 averages. The detection windows were set as 493 to 556 nm for green and 615 to 741 nm for red. Z-stack images were acquired using overlapping optical sectioning with thickness determined by 1 Airy unit, with the maximum possible Z-stack height in order to assess tissue viability throughout the sample. We found that our extended staining protocol allowed the stain to diffuse throughout the biopsy, which made it possible to acquire a Z-stack covering the entire biopsy thickness (approximately 400 μm). Due to the time spent at room temperature on the microscope, the samples analyzed in this manner were not used for any HR-MAS data acquisition after imaging.

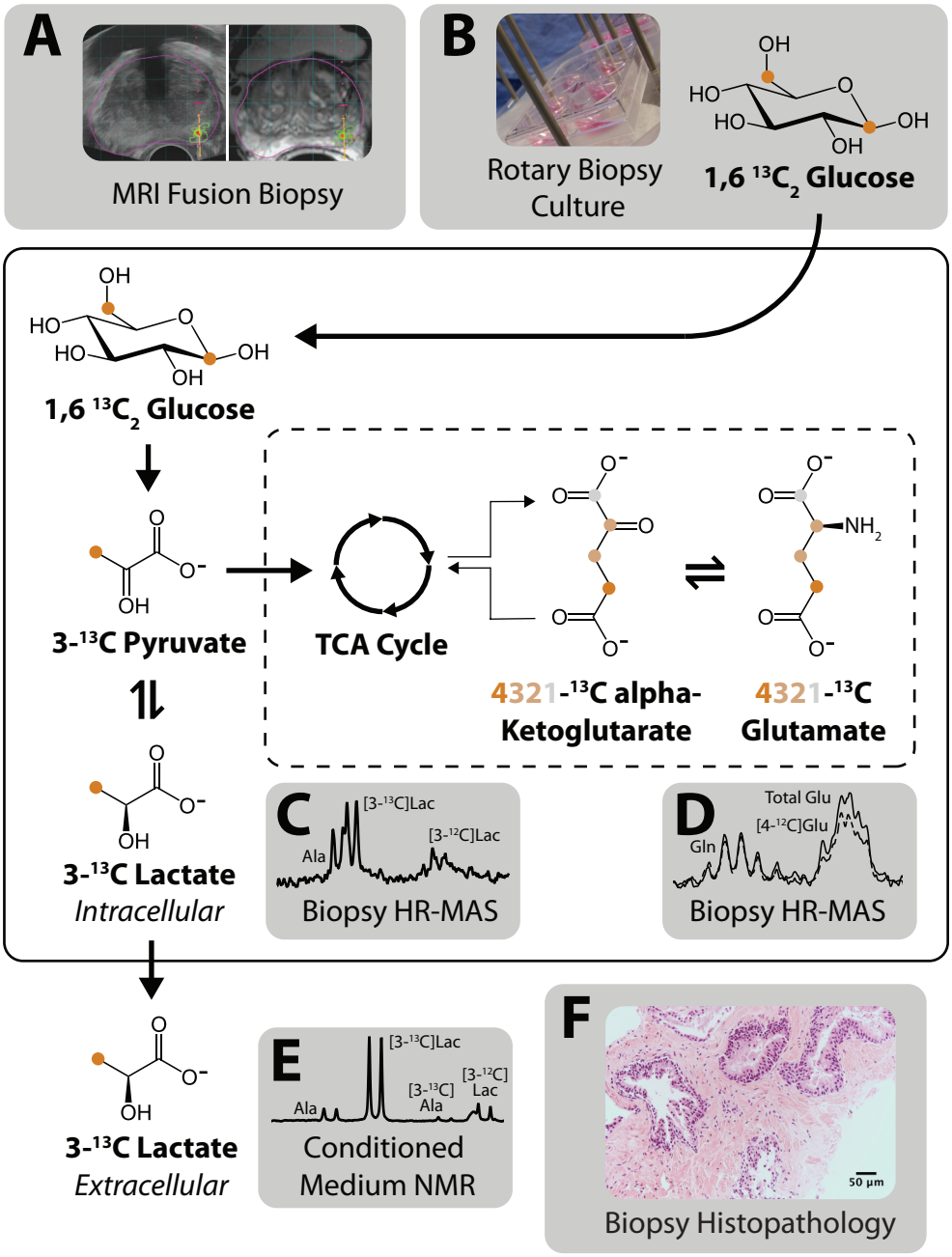

Figure 3.1. Biopsy labeling study protocol. A. MRI fusion biopsy was followed by B. rotary tissue culture with [1,6-$^{13}C_2$]glucose. C. Tissue lactate and D. glutamate concentration and fractional enrichment was quantified using HR-MAS of biopsy samples, whereas E. lactate efflux in media was quantified using NMR. F. The biopsy histopathology was obtained after culture.

Results

Overview of study protocol. The MRI fusion biopsy procedure provided registration of ultrasound to multiparametric prostate MRI, with the MRI lesion highlighted for biopsy targeting (Figure 3.1A). The freshly acquired biopsies were cultured with [1,6-$^{13}C_2$]glucose which was converted into [3-^{13}C]pyruvate via glycolysis (Figure 3.1B). The pyruvate interconverted with the intracellular lactate pool, which was quantified after culture using HR-MAS. Figure 3.1C: 500 MHz HR-MAS spectrum shows doublets of [3-^{12}C]alanine, [3-^{13}C]lactate, and [3-^{12}C]lactate going from left to right. Total scan time for this spectrum: 1 hour, 42 minutes. The pyruvate also entered the TCA cycle via pyruvate dehydrogenase, which led to labeling at the 4-position of alpha-ketoglutarate following one turn of the cycle. This interconverted with glutamate to produce labeling at the 4-position of glutamate. Figure 3.1D shows the higher amplitude of the multiplets corresponding to the C4 protons of glutamate when decoupling is turned on. Total scan time for this spectrum, with decoupling both off and on: 3 hours, 25 minutes. Figure 3.1E shows a representative spectrum of the media signifying the efflux of lactate and alanine from the biopsy tissue as evidenced by the ^{13}C satellite peaks of the respective methyl protons. The biopsy histopathology after culture demonstrated well-defined glands with preserved tissue microarchitecture. (Figure 3.1F: hematoxylin and eosin staining, 20× magnification.) The representative biopsy was benign with 30% glandular tissue and 70% stromal tissue (a detail of a glandular region is shown).

Study dataset. We obtained a total of 34 biopsies from 22 previously untreated patients. Of these biopsies, 16 were targeted to a radiologist-identified MRI lesion using

the MRI-ultrasound fusion biopsy device. Seven cancer biopsies and 27 benign biopsies were acquired. Among the benign biopsies, the average percentage of benign glandular tissue was 17% as determined by a board-certified genitourinary pathologist. Of the seven cancer biopsies, five had a Gleason score of 6(3+3) and two had a Gleason score of 7(3+4). The average percentage of cancer within the cancer biopsies was 12%, and the average percentage of benign glandular tissue was 9%.

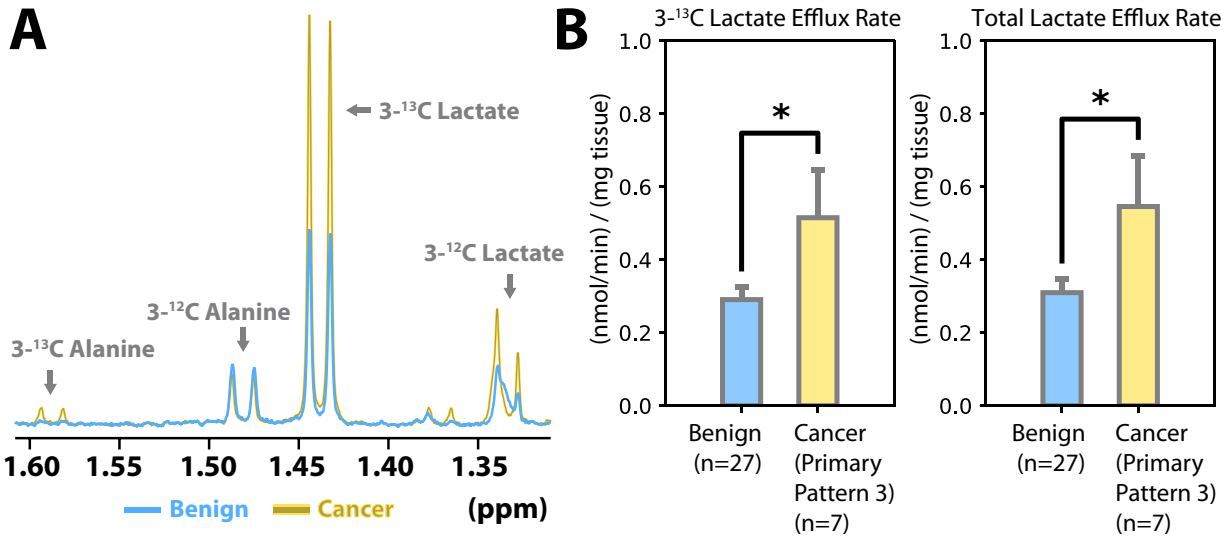

Figure 3.2. Biopsy lactate efflux and concentration. A. Representative NMR spectra from benign (blue) and cancer (yellow) media. The broad peak that is superimposed with the 3-^{12}C lactate doublet at 1.33 ppm is a medium additive that was deconvolved during the quantification process. B. Quantification of [3-^{13}C]lactate efflux and total lactate efflux in media. There was significantly greater [3-^{13}C]lactate and total lactate efflux in cancer biopsies compared to benign biopsies (p<0.05).

Biopsy media NMR measurements. We observed considerable efflux of [3-^{13}C]lactate into the medium during culture. In the representative NMR spectra normalized to tissue mass shown in Figure 3.2A, the cancer (yellow) medium after 24 hours of culture demonstrated a higher level of [3-^{13}C]lactate efflux compared to the benign (blue) medium.

As shown in Figure 3.2B, benign biopsies had a [3-^{13}C]lactate efflux rate of 0.29 ± 0.04 nmol/min/mg (mean ± standard error), whereas cancer biopsies had a [3-^{13}C]lactate efflux rate of 0.52 ± 0.14 nmol/min/mg measured over 24 hours in culture. Benign biopsies had a total lactate efflux rate of 0.31 ± 0.04 nmol/min/mg (mean ± standard error), whereas cancer biopsies had a total lactate efflux rate of 0.55 ± 0.14 nmol/min/mg measured over 24 hours in culture. Both the 3-^{13}C and total lactate efflux rates were significantly higher for the cancer biopsies ($p < 0.05$, two-tailed Student's *t*-test for independent samples). The fractional enrichment of the effluxed lactate was 95 ± 1 percent for benign biopsies and 94 ± 1 percent for cancer biopsies, with no significant fractional enrichment differences observed between benign and cancer biopsies.

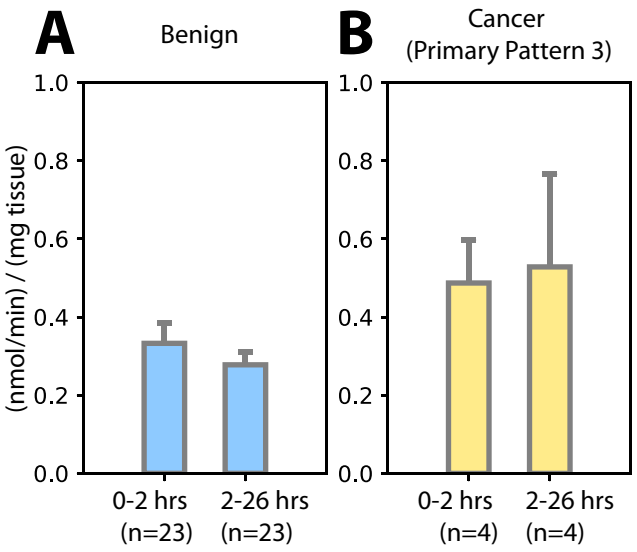

Figure 3.3. Biopsy lactate efflux over time. The biopsy lactate efflux rate per minute was measured from conditioned medium samples collected after two hours in culture ("0-2 hrs") and again from the same biopsies collected after a further 24 hours in culture ("2-26 hrs").

In an effort to assess the stability of lactate efflux over time in culture, for the majority of biopsies the lactate efflux rate per minute was measured from media collected after two hours of biopsy culture (“0-2 hrs”) and again from media collected after a further 24 hours of biopsy culture (“2-26 hrs”). We did not observe significant differences between the lactate efflux rates measured over these two timepoints (Figure 3.3A: benign 0-2 hrs: 0.33 ± 0.05 nmol/min/mg, benign 2-26 hrs: 0.28 ± 0.03 nmol/min/mg. Figure 3.3B: cancer 0-2 hrs: 0.49 ± 0.10 nmol/min/mg, cancer 2-26 hrs: 0.53 ± 0.23 nmol/min/mg.)

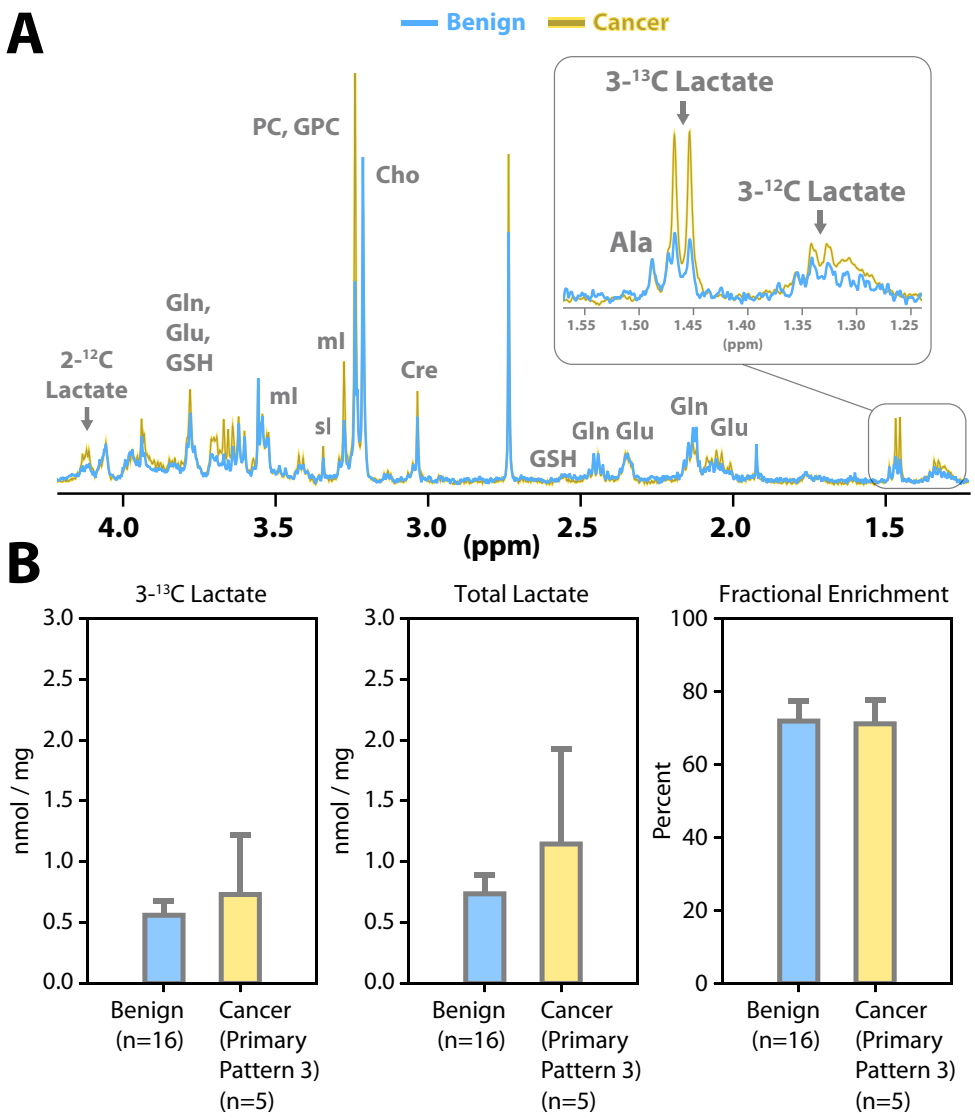

Figure 3.4. Biopsy tissue HR-MAS spectra. A. Example CPMG spectra from benign (blue) and cancer (yellow) samples after culture. The [2-^{12}C]lactate peak is visible at left, as a quartet split by the long-range coupling (~4 Hz) to [3-^{13}C]lactate. Ala: alanine, Glu: glutamate, Gln: glutamine, GSH: glutathione, Cre: creatine, Cho: choline, PC: phosphocholine, GPC: glycerophosphocholine, mI: *myo*-inositol, sI: *scyllo*-inositol. B. Quantified CPMG data: [3-^{13}C]lactate concentration, total lactate concentration, and fractional enrichment of lactate at the 3-position.

Biopsy tissue NMR measurements. Of the 34 biopsies cultured during this study, 7 were used for non-HR-MAS experiments after culture and 6 were not measured by HR-MAS due to technical issues. We obtained high-quality HR-MAS data from 21

biopsies suitable for metabolite quantification. Of these HR-MAS samples, 16 were benign, four were Gleason score 6(3+3) and one was Gleason score 7(3+4). It was possible to observe a number of metabolites in the HR-MAS CPMG spectra from biopsy tissues after culture, including metabolites that we have previously quantified in prostate tissue such as phospholipids[70] (Figure 3.4A). However, the focus of the present study was lactate production and efflux in culture. Despite a trend towards higher lactate levels in the cancer biopsies, we did not observe significant differences between benign and cancer biopsies after culture (Figure 3.4B). The [3-^{13}C]lactate concentration after culture was 0.56 ± 0.12 nmol/mg (mean ± standard error) in benign biopsies and 0.73 ± 0.49 nmol/mg in cancer biopsies. The total lactate concentration after culture was 0.74 ± 0.15 nmol/mg (mean ± standard error) in benign biopsies and 1.15 ± 0.78 nmol/mg in cancer biopsies. The fractional enrichment was 72 ± 6 % in benign biopsies and 71 ± 6 % in cancer biopsies.

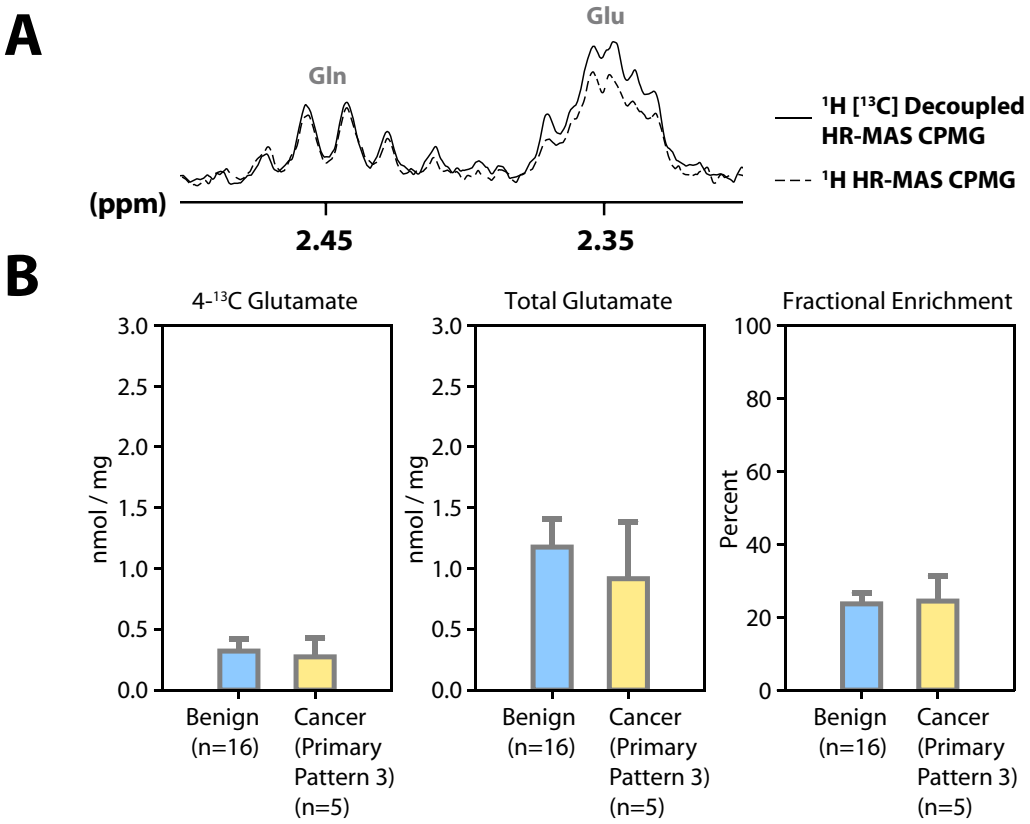

Figure 3.5. Labeling of glutamate from glucose. A. There is an increase of the glutamate C4 multiplet amplitude at 2.34 ppm with ^{13}C decoupling turned on, indicating fractional enrichment. B. Quantified CPMG data: 4-^{13}C glutamate concentration, total glutamate concentration, and fractional enrichment of glutamate at the 4-position.

Labeling of glutamate from [1,6-$^{13}C_2$]glucose. We were able to detect an increase of the glutamate C4 multiplet amplitude at 2.34 ppm with ^{13}C decoupling turned on, indicating fractional enrichment (representative spectrum, Figure 3.5A). However, no significant differences were observed between the benign and cancer (primary pattern 3) biopsies in terms of the glutamate concentration and/or fractional enrichment (Figure 3.5B). As shown in Figure 3.5B, the [4-^{13}C]glutamate concentration after culture was 0.32 ± 0.10 nmol/mg (mean ± standard error) in benign biopsies and 0.27 ± 0.15 nmol/mg in cancer biopsies. The total glutamate concentration after culture was 1.18 ±

0.23 nmol/mg in benign biopsies and 0.92 ± 0.47 nmol/mg in cancer biopsies. The fractional enrichment of C4 glutamate after culture was 24 ± 3 percent in benign biopsies and 24 ± 7 percent in cancer biopsies.

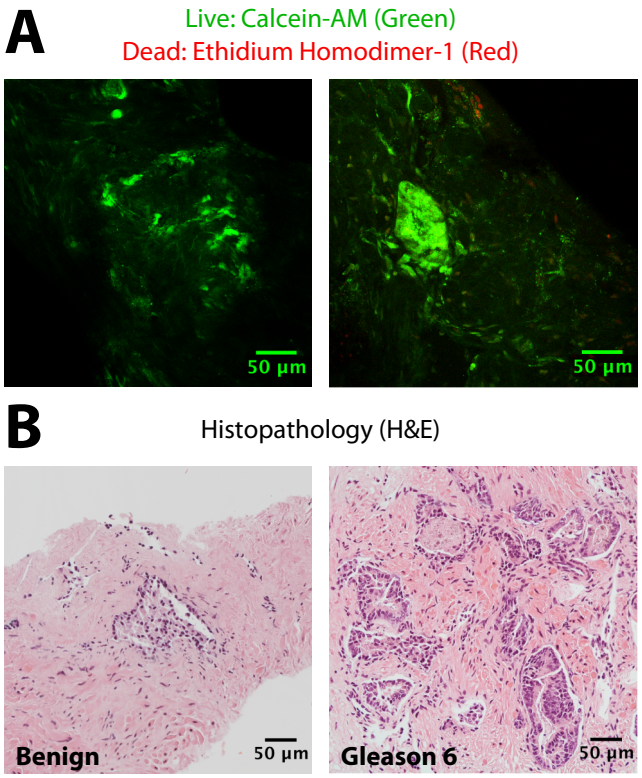

Figure 3.6. Biopsy LIVE/DEAD staining. A. Confocal two-photon microscopy from biopsy samples stained with calcein-AM and ethidium homodimer-1 following 26 hours in culture. B. Biopsy histopathology obtained after confocal microscopy. Each hematoxylin and eosin (H&E) stained image originates from the same sample as the confocal image directly above, but not from the exact same location in the tissue.

Biopsy LIVE/DEAD staining. We assessed the biopsy viability after 26 hours in rotary culture using a fluorescent vital stain that is trapped in living cells (Calcein-AM) combined with a nuclear stain that enters the nuclei of dead cells (ethidium homodimer-1). Scattered stromal cells demonstrated staining with ethidium homodimer-1, but the biopsies were primarily stained by the calcein-AM (Figure 3.6A), indicating that the majority of cells remained viable in biopsies after culture. The corresponding

histopathology slides further demonstrated intact glandular architecture after culture (Figure 3.6B).

Discussion

In this study, we found that it was possible to perform NMR measurements of metabolism in individual living human prostate biopsies. Furthermore, the ^{13}C-labeled and overall rates of lactate efflux in culture were significantly higher for low-grade (primary Gleason pattern 3) cancer biopsies as compared to benign biopsies (Figure 3.2). In the HR-MAS data (Figure 3.4), for benign biopsies we observed a tissue lactate concentration of 0.74 ± 0.15 nmol/mg, in good agreement with a prior published measurement of 0.61 ± 0.28 nmol/mg in snap-frozen biopsy samples.[10] For cancer biopsies, we observed a tissue lactate concentration of 1.15 ± 0.78 nmol/mg, as compared to a prior measurement of 1.59 ± 0.61 nmol/mg in snap-frozen cancer biopsies.[10] This discrepancy can perhaps be explained by the fact that the present dataset contained only low grade prostate cancer biopsies (primary Gleason pattern 3), whereas the dataset from Tessem et al. contained specimens of low and high grade prostate cancer (primary Gleason patterns 3 and 4). These findings are consistent with the notion that there is a more pronounced Warburg effect in high grade prostate cancer such as primary Gleason pattern 4.[71]

In an earlier study of prostate tissue slices derived from surgical specimens, the fractional enrichment of lactate following two hours of culture with [3-^{13}C]pyruvate was between 6 and 16 percent.[17] In that study, the [3-^{13}C]pyruvate label going to C3 lactate was most likely diluted by the presence of unlabeled glucose in the culture medium. In

the present work, we employed [1,6-$^{13}C_2$]glucose as the metabolic labeling substrate and we used a culture medium without pyruvate, which generated a higher fractional enrichment of lactate. In general, the relative contributions of media glucose and pyruvate to the tissue lactate pool are expected to depend upon the relative expression levels of membrane-located GLUT and MCT transporters, as well as the LDH isoform pattern, the redox state of the cell, and the relative rates of glycolysis and oxidative phosphorylation.[17]

Interestingly, while a significant difference in tissue lactate fractional enrichment coming from [1,6-$^{13}C_2$]glucose was not observed, the overall rate of lactate efflux in culture was significantly higher for primary Gleason pattern 3 cancer biopsies as compared to benign biopsies. This was presumably due to not only the trend toward higher lactate pool size, but also the propensity of the cancer tissue to export the lactate (Figure 3.2). This is consistent with prior data showing overexpression of the lactate dehydrogenase-A (LDHA) isoform (favoring lactate production from pyruvate) as well as overexpression of the monocarboxylate transporter MCT4, favoring lactate efflux, in human prostate cancer tissue compared to benign prostatic tissue.[17] Moreover, prior studies have shown that both increasing expression of MCT4 mRNA as well as MCT4 protein (quantified via immunohistochemistry) pathologically correlate with higher Gleason score, suggesting that lactate efflux from prostate biopsies would provide a sensitive assessment of aggressive disease.[72,73,74,75]

In this study, a longer duration of [1,6-$^{13}C_2$]glucose labeling was utilized in culture in order to yield a media [3-^{13}C]lactate peak with higher SNR. It was therefore important to demonstrate that the rate of lactate efflux did not change over time, and in this study

the lactate efflux rate was not significantly different at late (2 to 26 hours) vs. early (0 to 2 hours) time points (Figure 3.3). Theoretically, it would also be possible to increase the lactate concentration (and hence lactate SNR) effluxed into the media by decreasing the medium volume that is used during culture. However, we used a rotary tissue culture system that relies upon a 2.5 mL media volume within a 6-well plate to provide optimal exposure to medium and 5% CO_2 / 21% O_2 air. In our experience (data not shown), alternatives such as 24-well plates do not yield the same level of tissue viability, and would need to be further optimized to provide the correct ratio of medium to air exposure over time. It is also possible to increase the SNR of dilute NMR metabolites via lyophilization[76]; however, using the presented protocol, we achieved sufficient media lactate SNR without additional sample processing.

The fractional enrichment of C4 glutamate coming from [1,6-$^{13}C_2$]glucose in the biopsies studied is an indication of TCA cycle activity during rotary biopsy culture (Figure 3.1, Figure 3.5). In the current work we obtained a C4 glutamate fractional enrichment of 24 percent, whereas in an earlier study of prostate tissue slices obtained from surgical specimens, the fractional enrichment of tissue C4 glutamate following two hours of culture with [3-^{13}C]pyruvate was between 10 and 14 percent.[17] In that study, the [3-^{13}C]pyruvate label going to C4 glutamate was most likely diluted by the presence of unlabeled glucose or a relatively lower uptake of pyruvate (in comparison to glucose) in the culture medium. The reported fractional enrichment values for C4 glutamate should be viewed as a balance between TCA cycle metabolism of [1,6-$^{13}C_2$]glucose as well as uptake of compounds that can contribute to the unlabeled tissue glutamate pool

such as glutamine and glutamate. The culture medium used for this study contained 1 mM glutamine and 0.1 mM glutamate (Supporting Information).

This study had a number of limitations. In particular, our goal was to develop the biopsy culturing and metabolic profiling protocol, so we focused on biopsies routinely acquired from patients undergoing active surveillance or workup for prostate-related symptoms who had not been previously treated. Due to the low prevalence of aggressive cancer in this population, we only obtained biopsies containing benign glands or primary Gleason pattern 3 cancer, which limited our ability to further characterize the metabolic phenotype of aggressive prostate cancer.

Conclusion

In summary, a protocol was developed that allowed the quantification of lactate production and efflux in single living human prostate biopsies (1-6 mg of tissue), as well as the potential to quantify TCA metabolism through the quantification of fractional enrichment of glutamate. This was accomplished by optimizing experimental parameters such as the duration of time in rotary tissue culture (24 hours) and the parameters of the NMR acquisition so as to achieve sufficient SNR from small metabolite signals within a 3 hours and 25 minutes HR-MAS acquisition time. Validation studies demonstrated that this optimized protocol provided measurements of lactate production/fractional enrichment and efflux consistent with prior data describing lactate pool size, LDHA and MCT4 expression in benign human prostatic tissue vs. prostate cancer.[10,17] Having established this protocol, similar measurements can then be

performed on treatment-resistant and/or metastatic prostate cancer biopsies for a better understanding of metabolic perturbations in the setting of aggressive prostate cancer.

Acknowledgement

We wish to thank Professor Matthew Merritt of the University of Florida for useful discussions. Romelyn Delos Santos tirelessly processed all of the biopsy samples for pathology reading by Dr. Laura Tabatabai of the UCSF Department of Pathology. Rosalie Nolley of Stanford University prepared the biopsy medium ingredients on countless occasions. Current and former members of the UCSF Radiology team including Justin Delos Santos, Vahid Ravanfar, Fariba Ravanfar, and Christine Larson were a pleasure to work with when consenting patients. Dr. Katsuto Shinohara, Dr. Hao Nguyen, and Dr. Matthew Cooperberg of the UCSF Department of Urology were of utmost assistance in obtaining the biopsy samples, as were the vocational nurses Selvi Johnson, Yanira Rafael, Trinidad Gleave, and Jasmine Meidinger. Jinny Sun, Renuka Sriram, Donna Peehl, and my adviser Professor John Kurhanewicz provided essential guidance, feedback and suggestions. Anna Celli and Sarah Elmes of the Laboratory for Cell Analysis at UCSF provided access and training for the Zeiss 780 laser scanning confocal microscope. Mark Kelly of the UCSF NMR lab was an extremely patient and cheerful resource at all times. Subramaniam Sukumar and Mark VanCriekinge provided essential training and technical assistance for HR-MAS studies. DeLaine Larsen of the Nikon Imaging Center at UCSF provided training and assistance on the 6D microscope. Finally, and most importantly, we wish to thank the patients who generously donated their tissue for this project.

Supporting Information

Table 3.1. Culture medium formulation.

Compound	Formula	mg/L
Metabolic Tracers		
1,6 $^{13}C_2$ glucose	$^{13}C_2C_4H_{12}O_6$	1011.01
Growth Factors		
Bovine pituitary extract	Multiple components	40
Cholera toxin	Protein	0.01
Epidermal growth factor	Protein	0.01
Gentamicin sulfate	$C_{60}H_{125}N_{15}O_{25}S$	100
Hydrocortisone	$C_{21}H_{30}O_5$	1
Insulin	Protein	4
Phosphoethanolamine	$C_2H_8NO_4P$	14
R1881	$C_{19}H_{24}O_2$	0.014
Retinoic acid	$C_{20}H_{28}O_2$	0.00001
Selenous Acid	H_2SeO_3	0.0024
Vitamin E	$C_{29}H_{50}O_2$	0.99
Inorganic Salts		
Calcium chloride (anhydrous)	$CaCl_2$	168.2
Cupric sulfate·$5H_2O$	$CuSO_4 \cdot 5H_2O$	0.00249
Ferrous sulfate·$7H_2O$	$FeSO_4 \cdot 7H_2O$	1.634
Magnesium chloride·$6H_2O$	$MgCl_2 \cdot 6H_2O$	228.60
Magnesium sulfate·$7H_2O$	$MgSO_4 \cdot 7H_2O$	39.4
Potassium chloride	KCl	223.60
Sodium bicarbonate	$NaHCO_3$	1176.00
Sodium chloride	NaCl	7599.00
Sodium phosphate, heptahydrate	$Na_2H_2PO_4 \cdot 7H_2O$	268.00
Zinc sulfate·$7H_2O$	$ZnSO_4 \cdot 7H_2O$	1.003
Other Components		
Hypoxanthine	$C_5H_4N_4O$	4.10
Linoleic acid	$C_{18}H_{32}O_2$	0.084
Lipoic acid	$C_8H_{14}O_2S_2$	0.21
Putrescine·2HCl	$C_4H_{14}Cl_2N_2 \cdot 2HCl$	0.161
Thymidine	$C_{10}H_{14}N_2O_5$	0.73

Compound	Formula	mg/L
Amino Acids		
L-Alanine	$C_3H_7NO_2$	8.90
L-Arginine hydrochloride	$C_6H_{14}N_4O_2 \cdot HCl$	211.00
L-Asparagine·H_2O	$C_4H_8N_2O_3 \cdot H_2O$	15.01
L-Aspartic acid	C4H7NO4	13.30
L-Cysteine hydrochloride·H_2O	$C_3H_7NO_2S \cdot H_2O$	35.12
L-Glutamic acid	$C_5H_9NO_4$	14.70
L-Glutamine	$C_5H_{10}N_2O_3$	146.00
Glycine	$C_2H_5NO_2$	7.50
L-Histidine hydrochloride·H_2O	$C_6H_9N_3O_2 \cdot HCl \cdot H_2O$	20.96
L-Isoleucine	$C_6H_{13}NO_2$	3.94
L-Leucine	$C_6H_{13}NO_2$	13.10
L-Lysine·HCl	$C_6H_{14}N_2O_2 \cdot HCl$	36.50
L-Methionine	$C_5H_{11}NO_2S$	4.48
L-Phenylalanine	$C_9H_{11}NO_2$	4.96
L-Proline	$C_5H_9NO_2$	34.50
L-Serine	$C_3H_7NO_3$	10.50
L-Tryptophan	$C_{11}H_{12}N_2O_2$	2.04
L-Tyrosine	$C_9H_{11}NO_3$	5.40
L-Valine	$C_5H_{11}NO_2$	11.70
Vitamins		
Biotin	$C_{10}H_{16}N_2O_3S$	0.0073
D-Calcium pantothenate	$C_{18}H_{32}CaN_2O_{10}$	0.48
Choline chloride	$C_5H_{14}ClNO$	13.96
Folic acid	$C_{19}H_{19}N_7O_6$	1.30
i-Inositol	$C_6H_{12}O_6$	18.00
Niacinamide	$C_6H_6N_2O$	0.037
Pyridoxine hydrochloride	$C_8H_{11}NO_3 \cdot HCl$	0.062
Riboflavin	$C_{17}H_{20}N_4O_6$	0.038
Thiamine HCl	$C_{12}H_{17}ClN_4OS \cdot HCl$	0.34
Vitamin B_{12}	$C_{63}H_{88}CoN_{14}O_{14}P$	1.36

Table 3.2. Sources of culture medium ingredients.

Component/Chemical	Vendor	Catalog Number
L-alanine	Sigma Aldrich St. Louis, MO	A7627
L-arginine - HCl	Sigma Aldrich St. Louis, MO	A5131
l-asparagine	Sigma Aldrich St. Louis, MO	A0884
L-aspartate	Sigma Aldrich St. Louis, MO	A9256
biotin	Sigma Aldrich St. Louis, MO	B5401
bovine pituitary extract	Hammond Cell Tech, Santa Rosa, CA	1078-NZ
$CaCl_2 \cdot 2H_20$	Sigma Aldrich St. Louis, MO	C3881
calcium panthothenate	Sigma Aldrich St. Louis, MO	P2250
cholera toxin	List Biological, Campbell, CA	101
choline chloride	Sigma Aldrich St. Louis, MO	C7017
$CuSO_4 \cdot 5H_2O$	Sigma Aldrich St. Louis, MO	C7631
L-cystine	Sigma Aldrich St. Louis, MO	C8755
epidermal growth factor	Collaborative Research, Waltham, MA	40001
$FeSO_4 \cdot 7H_2O$	Sigma Aldrich St. Louis, MO	F7002
folic acid	Sigma Aldrich St. Louis, MO	F7876
gentamycin	United States Biochemical Corp, Cleveland, OH	16051
glucose	Sigma Aldrich St. Louis, MO	D9434
L-glutamate	Sigma Aldrich St. Louis, MO	G1251
L-glutamine	Sigma Aldrich St. Louis, MO	G3126
glycine	Sigma Aldrich St. Louis, MO	G7126
Hepes	Sigma Aldrich St. Louis, MO	H3375
L-histidine - HCl $-H_20$	Sigma Aldrich St. Louis, MO	H8125
hydrocortisone	Sigma Aldrich St. Louis, MO	H4001
hypoxanthine	Sigma Aldrich St. Louis, MO	H9377
Insulin	Collaborative Research, Waltham, MA	40205
L-isoleucine	Sigma Aldrich St. Louis, MO	I2752
KCl	Sigma Aldrich St. Louis, MO	P4504
L-leucine	Sigma Aldrich St. Louis, MO	L8000
L-lysine - HCl $-H_20$	Sigma Aldrich St. Louis, MO	L5626
$MgCl_2 \cdot 6H_2O$	Sigma Aldrich St. Louis, MO	M0250
$MgSO_4 \cdot 7H_2O$	Sigma Aldrich St. Louis, MO	M1880
L-methionine	Sigma Aldrich St. Louis, MO	M9625
myo - inositol	Sigma Aldrich St. Louis, MO	I5125
niacinamide	Sigma Aldrich St. Louis, MO	N3376
phenol red -Na salt	Sigma Aldrich St. Louis, MO	P4758
l-phenylalanine	Sigma Aldrich St. Louis, MO	P2126
phosphoethanolamine	Calbiochem, San Diego, CA	5248

Component/Chemical	Vendor	Catalog Number
KH_2PO_4	Sigma Aldrich St. Louis, MO	P5655
L-proline	Sigma Aldrich St. Louis, MO	P0380
putrescine-2HCl	Sigma Aldrich St. Louis, MO	P5780
pyrodoxine - HCl	Sigma Aldrich St. Louis, MO	P9755
R1881	Sigma Aldrich St. Louis, MO	R0908
retinoic acid	Sigma Aldrich St. Louis, MO	R2625
riboflavin	Sigma Aldrich St. Louis, MO	R4500
selenium	Sigma Aldrich St. Louis, MO	211176
L-serine	Sigma Aldrich St. Louis, MO	54500
NaCl	Sigma Aldrich St. Louis, MO	S7653
$Na_2HPO_4 \cdot 7H_2O$	J T Baker, Phillipsburg, NJ	I-3824
$NaHCO_3$	Sigma Aldrich St. Louis, MO	S5761
sodium pyruvate	Sigma Aldrich St. Louis, MO	P2256
L-threonine	Sigma Aldrich St. Louis, MO	T8625
thiamine - HCl	Sigma Aldrich St. Louis, MO	T4625
6,8 - thioctic acid	Sigma Aldrich St. Louis, MO	T5625
thymidine	Sigma Aldrich St. Louis, MO	T9250
L-tryptophan	Sigma Aldrich St. Louis, MO	T0254
L-tyrosine	Sigma Aldrich St. Louis, MO	T3754
vitamin B12	Sigma Aldrich St. Louis, MO	V2876
vitamin E	Sigma Aldrich St. Louis, MO	T1539
L-valine	Sigma Aldrich St. Louis, MO	V0500
$ZnSO_4 \cdot 7H_2O$	Sigma Aldrich St. Louis, MO	Z4750

Biopsy tissue NMR measurements: automated HR-MAS shimming routine. Each of the shim groups in this list was iteratively adjusted, and the shim setting corresponding to the maximum FID area was selected by the algorithm as the starting point for the adjustment of the next shim group in the list.

1. z1 z2 x1 y1 xz yz xy x2y2
2. xz yz xz2 yz2
3. z1 z2 x1 y1 xz yz xy x2y2
4. z1 z2 x1 y1

Biopsy media NMR measurements: automated shimming routine. Initially, a shim milestone was acquired using the 3D Bruker Topshim routine via the TopSpin command: “topshim 3dfast ordmax=8,8 convcomp tunea”.
Subsequently, the lineshape was refined for each individual media sample using the command: “topshim ordmax=8 convcomp tunea”.

Chapter 4. HR-MAS CPMG and HSQC Quantification of Metabolism in Human Prostate Tissue Slice Cultures Labeled with [1,6-$^{13}C_2$]Glucose or [3-^{13}C]Glutamine

Introduction

In the United States, men with primary prostate cancer are treated with radical prostatectomy (RP), with radiation therapy (RT) reserved for high Gleason grade and/or locally invasive cases. After this treatment the serum prostate-specific antigen (PSA) level is expected to drop to zero, and a serum PSA level significantly greater than zero is defined as a biochemical recurrence.[77] The mainstay of treatment for biochemically recurrent prostate cancer is androgen deprivation therapy (ADT) using centrally acting agents (i.e. leuprolide and flutamide).[77] Recent randomized-controlled trial evidence has demonstrated that peripherally acting androgen receptor inhibitors (i.e. abiraterone,[78] enzalutamide,[79] and apalutamide[80]) are highly efficacious when added to ADT early in the disease course, with median metastasis-free survival between 36 and 40 months when androgen receptor inhibitor therapy is initiated in the non-metastatic setting.[79,80] Rising PSA and/or metastasis in the setting of ADT and androgen receptor inhibition is compatible with a diagnosis of castration-resistant prostate cancer (CRPC). Hence, CRPC is a subject of considerable research interest,[20,21] because it is the primary mode of treatment escape and lethality in prostate cancer.

Recently, it has been recognized that CRPC can transdifferentiate to neuroendocrine prostate cancer (NEPC) under the influence of androgen receptor inhibition.[81,82,83] Unlike the comparatively rare *de novo* NEPC, treatment-induced NEPC represents a significant minority of treatment-resistant prostate cancer cases, with N-Myc amplification as a common feature of NEPC.[82] This fact is of particular interest for

the field of tumor metabolism, because Myc is a master regulator of glycolysis as well as glutaminolysis.[22,23] Thus, there is potential for metabolic imaging strategies such as hyperpolarized ^{13}C MRI based upon [1-^{13}C]pyruvate, [2-^{13}C]pyruvate and/or [5-^{13}C]glutamine to noninvasively detect the emergence of NEPC in patients undergoing androgen receptor inhibition.[84] This, in turn could potentially enable personalized therapeutic selection targeting NEPC-specific genomic alterations.

The capability to noninvasively assess the rates of glycolysis and glutaminolysis in vivo is impacted by hyperpolarized (HP) probe polarization, probe transport, and fractional enrichment going from precursor to product.[64] Prior work has assessed the metabolism of glucose and glutamine in preclinical models of human neuroendocrine prostate cancer and in human prostate tissue using mass spectrometry-based metabolomics[85] as well as gene set enrichment analysis (GSEA) of transcriptomic data from patient-derived xenografts.[86] However, given the multiple layers of regulation and intersecting metabolic pathways that are present in the prostate cancer cell, it is not always possible to directly infer metabolic fluxes from metabolomic pool sizes, nor from gene expression information.

In this work, employing a previously developed and validated rotary tissue culture system for primary living human prostate tissue,[17] we set out to directly measure the fractional enrichment of key downstream metabolites such as glutamate, coming from the labeled precursors [1,6-$^{13}C_2$]glucose or [3-^{13}C]glutamine. The tissue samples for this study came from patients with treatment-naïve prostate cancer undergoing radical prostatectomy. Thus, our goal was to better characterize glucose and glutamine

metabolism in treatment-naïve human prostate cancer while developing a protocol that would be suitable for future work in samples of CRPC and/or NEPC.

Materials and Methods

Tissue collection. Prostate cancer patients undergoing radical prostatectomy (RP) as part of their standard clinical care consented to participate in an IRB-approved study involving fresh tissue collection. Following RP, the whole prostate specimen was brought to the gross pathology lab by a trained genitourinary gross pathology technician. The specimen was weighed and then partially sectioned at the level of the midgland to expose the interior of the gland while maintaining intact margins. Tumor(s) were cored using a 5 mm or 8 mm coring tool depending on tumor size (Alabama R&D, Inc.) while maintaining intact margins. When available, a benign area of the prostate gland was additionally cored. The tumor cores were placed in Hank's Buffered Saline Solution (HBSS) on ice.

Tissue core slicing. Fresh tissue cores were immersed in chilled HBSS and sliced on a fresh tissue slicer (Alabama R&D, Inc.) with a target slice thickness of 350 µm verified using a thickness gauge.

Rotary tissue culture. Tissue slices were allowed to recover overnight for 16 to 24 hours in 6-well plates on a rotary tissue culture system (Alabama R&D, Inc.) within a 37 °C, 5% CO_2 incubator. The medium used was PFMR-4a with prostate-specific additives as described previously.

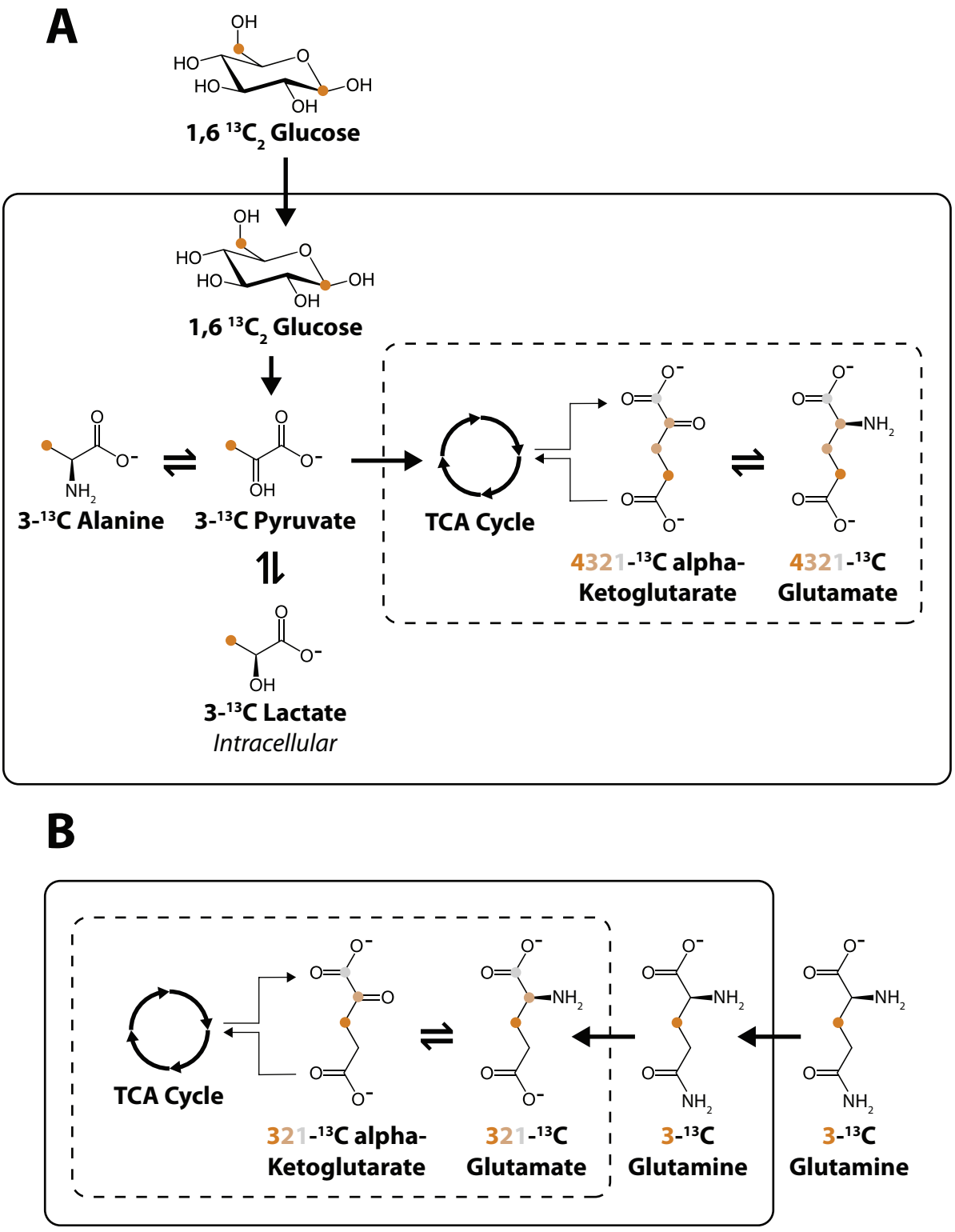

Figure 4.1. Tissue slice labeling substrates and metabolic pathways. Each tissue slice was labeled with either (A) [1,6-$^{13}C_2$]glucose or (B) [3-^{13}C]glutamine.

Metabolic labeling. The next day, prostate tissue slices were transferred to a new culture medium well for either glucose or glutamine labeling. The labeling medium was F-12 without HEPES or pyruvate, with prostate medium additives included as described in Chapter 3. The glucose labeling wells contained [1,6-$^{13}C_2$]glucose at 1.011 g/L (5.55 mM) with 5 mM of unlabeled glutamine. As shown in Figure 4.1A, the [1,6-$^{13}C_2$]glucose ^{13}C labels were expected to generate [3-^{13}C]alanine and [3-^{13}C]lactate in addition to [4-^{13}C]glutamate, [3-^{13}C]glutamate, and [2-^{13}C]glutamate after successive turns of the tricarboxylic acid (TCA) cycle. The glutamine labeling wells contained unlabeled glucose at 0.9999 g/L (5.55 mM) with 1 mM of unlabeled glutamine and 4 mM of labeled [3-^{13}C]glutamine. As shown in Figure 4.1B, the [3-^{13}C]glutamine ^{13}C label was expected to generate [3-^{13}C]glutamate as well as [2-^{13}C]glutamate after one turn of the tricarboxylic acid (TCA) cycle. Following 8 hours in labeling culture, the tissue slices were individually immersed in cold phosphate-buffered saline (PBS), blotted using a kimwipe, and stored at –80 °C.

Extended metabolic labeling. As a supplemental experiment, to assess the potential for increased metabolic labeling over time, limited numbers of samples were labeled with either [1,6-$^{13}C_2$]glucose or [3-^{13}C]glutamine for 24 hours instead of 8 hours.

Tissue NMR procedure. Tissue slices were loaded into a sealed zirconium HR-MAS rotor on a tared digital balance to measure the wet tissue weight. Three µL of D_2O/0.05% trimethylsilylpropanoic acid (TSP) solution was further added to the rotor and weighed. After this, three µL of D_2O containing [2-^{13}C]glycine at 17 mM was added to the rotor and weighed.[65] The glycine was employed as a reference standard for heteronuclear single quantum coherence (HSQC) experiments. The HR-MAS rotor was

sealed and loaded into a 500 MHz Varian gHX Nano (proton-carbon double resonance) 4 mm indirect detection HR-MAS probe maintained at 1 °C. Acquisition was performed at a spin rate of 2.25 kHz using a Varian Inova console with VNMRJ 4. The probe tuning, 90° pulse width and water saturation frequency were calibrated for each sample. Each sample was shimmed using an automated FID shimming routine for 45 minutes.

Tissue CPMG sequence. Locked ^{1}H Carr-Purcell-Meiboom-Gill (CPMG) spectra were acquired with 60,000 complex points, 3 second acquisition time, 2 second water suppression pulse, 6 second overall repetition time, and 256 scans. It was previously established that this repetition time yielded fully relaxed spectra in human prostate tissue.[35] The CPMG echo time was set to 288 ms. The spacings of 180° pulses within the CPMG sequence were synchronized to the spinning period of the rotor. To quantify metabolite total pools in addition to ^{13}C labeled pools, CPMG datasets were acquired both with and without heteronuclear ^{13}C decoupling using a GARP pulse for a total CPMG scan time of 51 minutes, 12 seconds.

Tissue HSQC sequence. The proton-carbon tissue heteronuclear single quantum coherence (HSQC) sequence, used to quantify ^{13}C-labeled metabolites, consisted of a standard INEPT … 180° … reverse INEPT train with a two-second presaturation lobe. The overall repetition time (TR) was 3 seconds. The acquisition time was 0.444 seconds with 4,444 complex points, corresponding to a spectral window in F_2 (proton) of 10,000 Hz or 20 ppm at 500 MHz. There were 256 increments acquired in t_1. The spectral window in F_1 (carbon) was 9,046.7 Hz or 72 ppm. The INEPT delay time was set to 1.777 ms, synchronized to four revolutions of the HR-MAS rotor at a spin rate of 2.25 kHz. This yielded a J_{CH} filter value of 1/(4*1.777 ms) or 140.625 Hz. The free induction

decay (FID) was acquired with heteronuclear ^{13}C decoupling using a GARP pulse. There were 12 averages acquired, for a total scan time of 5 hours and 10 minutes.

Tissue histopathology. Following the HR-MAS data acquisition, the tissue samples were fixed in 10% neutral-buffered formalin, embedded in paraffin, sectioned, and stained with hematoxylin and eosin (H&E) and high-molecular weight cytokeratin for interpretation by a board-certified genitourinary pathologist. For each sample the pathologist determined the primary Gleason pattern, secondary Gleason pattern, Gleason score, percentage of cancer, percentage of glandular tissue, and percentage of stromal tissue.

Tissue CPMG processing and quantification. All CPMG datasets were processed in MestreNova 12 (Mestrelab Research S.L.). The datasets were zero-padded by a factor of 2, apodized with a 0.25 Hz exponential filter and automatically phased and baselined using a Whittaker smoother algorithm. Dataset phases were manually refined, and automatic baselines were replaced with manual baselining in cases where the automatic results were not acceptable. Peaks of interest were automatically picked and fitted using a Lorentzian-Gaussian shape function with a simulated annealing algorithm (500 coarse iterations, 100 fine iterations, and a local minima filter of 25 were used). All automated peak fits were visually assessed for fit quality and adjusted when necessary. In the tissue HR-MAS CPMG data, peak areas were quantified relative to the calibrated amplitude of the Electronic REference To access In vivo Concentrations (ERETIC) signal, corrected for the number of metabolite protons.[66] Appropriate T_2 corrections were applied based upon HR-MAS measurements using a CPMG sequence in human prostate tissue at 1 °C and 500 MHz (Table 4.1). Metabolite amounts were further

standardized by the wet tissue weight of the sample, to yield a tissue metabolite concentration in (nmol / mg).

Table 4.1. Metabolite ^{1}H T_1, ^{1}H T_2, and J_{CH} values. With the exception of glycine, which was used in solution as a reference standard, all metabolite T_1 and T_2 values were measured in prostate tissue at 1 °C and 500 MHz. The J_{CH} values are from solution.

Metabolite	Carbon	nH	T_1 (ms) [ref]	T_2 (ms) [ref]	J_{CH} (Hz) [ref]
Alanine	C3	3	500 [17]	208 [10]	130 [65]
Lactate	C3	3	425 [17]	251 [10]	128 [65]
Glutamine	C2	1	–	–	145.46 [87]
Glutamine	C3	2	–	–	131.36 [87]
Glutamine	C4	2	–	–	128.41 [87]
Glutamate	C2	1	–	–	145.14 [87]
Glutamate	C3	2	–	–	130.45 [87]
Glutamate	C4	2	530 [17]	275 [17]	126.79 [87]
Glycine	C2	2	1,309 [this work]	1,078 [this work]	143 [65]

Tissue HSQC processing and quantification. All HSQC datasets were processed in MestreNova 12 (Mestrelab Research S.L.). Datasets were zero-padded in F_1 from 256 to 2,048 points and were forward linear predicted using a Zhu-Bax algorithm with 231 points and 16 coefficients. The F_1 direction was apodized using a 10 Hz Gaussian filter. Datasets were zero-padded in $F2$ from 4,444 to 8,192 points and were apodized using a 1 Hz Gaussian filter. Datasets were automatically phased in both F_1 and F_2, with manual refinement as needed. Metabolites were quantified using ellipsoidal regions of integration. Metabolite integrals were corrected for J_{CH} filtering, longitudinal recovery, and number of protons, using the following equations.[88,89]

$$M'_{\mathrm{HSQC}} = \frac{M_{\mathrm{HSQC}}}{n(\mathrm{M})\sin^2\left(\frac{\pi J_{\mathrm{CH(M)}}}{2j_{1\mathrm{ch}}}\right)} \qquad (4.1)$$

$$\mathrm{Gly}'_{\mathrm{HSQC}} = \frac{\mathrm{Gly}_{\mathrm{HSQC}}}{n(\mathrm{Gly})\sin^2\left(\frac{\pi J_{\mathrm{CH(Gly)}}}{2j_{1\mathrm{ch}}}\right)} \frac{1}{1 - e^{\frac{-\mathrm{TR}}{T_1(\mathrm{Gly})}}} \qquad (4.2)$$

In Eq. (4.1) and (4.2), M_{HSQC} is the HSQC integral of an arbitrary metabolite M at a specific cross-peak, whereas M'_{HSQC} is the integral corrected for proton number and J_{CH} filtering. The parameter n(M) refers to the number of protons at that same cross-peak, referred to as nH in Table 4.1. The parameter $J_{CH(M)}$ refers to the single-bond carbon-proton coupling constant, also shown in Table 4.1. The parameter j_{1ch} refers to the J_{CH} filter value of the HSQC sequence, which was set to 140.625 Hz (INEPT delay = 1.777 ms, described above under "Tissue HSQC Sequence"). In Eq. (4.2), the glycine signal was additionally corrected for incomplete longitudinal recovery of its proton magnetization during HSQC acquisition[90] due to its comparatively long proton T_1 value measured in solution (Table 4.1). This procedure was not performed for the prostate tissue metabolites, because we expected that with shorter proton T_1 values in tissue (Table 4.1) the HSQC spectra would be fully relaxed at TR = 3 seconds.

Fractional enrichment calculation. Metabolite fractional enrichments were computed by taking the ratio of the ^{13}C-labeled metabolite pool from the HSQC dataset to the metabolite total pool from the ^{1}H[^{13}C] decoupled CPMG dataset. This ratio was accomplished by taking an internal ratio to the glycine area within each dataset after correcting for T_2 relaxation, as shown in Eq. (4.3), (4.4), and (4.5) below. Within the ^{1}H[^{13}C] decoupled CPMG dataset, metabolite pool size was determined using the C4 multiplet for glutamate, and using the C3 multiplets for alanine and lactate. These multiplets were selected for their relative freedom from contamination by other metabolites.

$$M'_{\text{hetnuc decoupled CPMG}} = \left(\frac{\exp\left(\frac{\text{TE}}{T_{2(\text{M})}}\right)}{n(\text{M})} \right) M_{\text{hetnuc decoupled CPMG}} \qquad (4.3)$$

$$\mathrm{Gly}'_{\text{hetnuc decoupled CPMG}} = \left(\frac{\exp\left(\frac{\mathrm{TE}}{T_{2(\mathrm{Gly})}}\right)}{n(\mathrm{Gly})} \right) \mathrm{Gly}_{\text{hetnuc decoupled CPMG}} \quad (4.4)$$

$$\mathrm{FE}_{(\mathrm{M})} = \frac{\frac{M'_{\mathrm{HSQC}}}{\mathrm{Gly}'_{\mathrm{HSQC}}}}{\frac{M'_{\text{hetnuc decoupled CPMG}}}{\mathrm{Gly}'_{\text{hetnuc decoupled CPMG}}}} \quad (4.5)$$

Oxygen consumption data acquisition. For a subset of samples, tissue oxygen consumption was measured using a calibrated Clark electrode (Oxygraph, Hansatech Instruments). The Oxygraph system requires that a magnetic stir bar be used to create efficient mixing of the tissue medium in the reaction cell. This stir bar rotation was more than sufficient to fragment and destroy prostate tissue, so we developed a customized 3D-printed tissue holder for the reaction cell. Tissue slices were removed from the incubator and weighed, and then oxygen consumption traces were acquired for 20 minutes. Control traces were acquired both before and after tissue oxygen consumption measurements in order to assess the background rate of oxygen consumption caused by the electrochemistry of the Clark electrode. This background rate was subtracted from all reported oxygen consumption measurements.

Oxygen consumption data processing. We found that small (<1 °C) periodic variations in water jacket temperature caused by the water heater created an oscillation in the Clark electrode current. A Python script was written to fit the slope of the Clark electrode reading over an integer number of heating cycles, so as to avoid bias in the resulting slope quantification. The resulting slope value was multiplied by the volume of tissue medium in the reaction cell and divided by the wet tissue weight to obtain a standardized oxygen consumption rate in terms of nmol O_2 / mg tissue / minute.

Results

Study dataset. We obtained a total of 35 prostate tissue slices from five patients. Among the samples labeled with [1,6-$^{13}C_2$]glucose, there were 11 cancer slices (n=8 Gleason 7(3+4) and n=3 Gleason 6(3+3) slices) and 6 benign slices. Among the samples labeled with [3-^{13}C]glutamine, there were 11 cancer slices (n=9 Gleason 7(3+4) and n=2 Gleason 6(3+3) slices) and 7 benign slices.

Labeling of alanine and lactate from [1,6-$^{13}C_2$]glucose. Figure 4.2A shows representative HSQC peaks for alanine C3 and lactate C3 from a cancer sample. As shown in Figure 4.2B, there was a non-significant trend towards increased alanine C3 fractional enrichment for cancer samples as compared to benign samples (in terms of mean ± standard error, 14 ± 2 % vs. 8 ± 3 %, p = 0.06, independent samples t-test). Similarly, there was a non-significant trend towards increased lactate C3 fractional enrichment for cancer samples as compared to benign samples (53 ± 4 % vs. 42 ± 7 %, p = 0.16). We did not observe significant differences between cancer and benign samples in terms of alanine and lactate concentrations after culture. The alanine concentration of cancer samples after culture was 0.55 ± 0.13 nmol/mg whereas the alanine concentration of benign samples was 0.42 ± 0.07 nmol/mg. The lactate concentration of cancer samples after culture was 2.26 ± 0.43 nmol/mg whereas the lactate concentration of benign samples was 1.99 ± 0.88 nmol/mg.

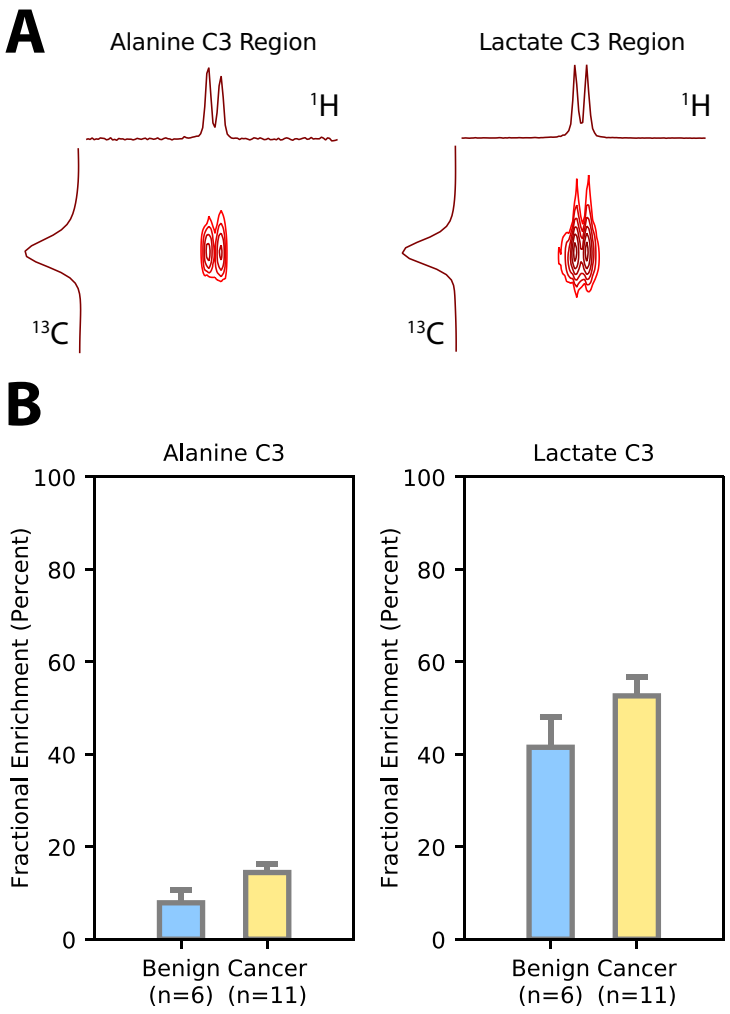

Figure 4.2. Labeling of alanine and lactate from [1,6-$^{13}C_2$]glucose. (A) Representative HSQC spectra with 1D slices taken through the central peaks. (B) Fractional enrichment.

Labeling of glutamate from [1,6-$^{13}C_2$]glucose. Figure 4.3A shows representative HSQC peaks for glutamate C4, C3, and C2 from a cancer sample labeled with [1,6-$^{13}C_2$]glucose. As shown in Figure 4.3B, there was a modestly significant trend towards increased glutamate fractional enrichment for cancer samples labeled with [1,6-$^{13}C_2$]glucose as compared to benign samples (glutamate C4: 14 ± 3 % vs. 8 ± 2%, p = 0.13; glutamate C3: 9 ± 2 % vs. 4 ± 1%, p = 0.04; glutamate C2: 8 ± 1 % vs. 4 ± 1%, p = 0.06). We did not observe significant differences between cancer and benign samples in

terms of glutamate concentration after culture. For the samples labeled with [1,6-$^{13}C_2$]glucose, the glutamate concentration of cancer samples after culture was 2.15 ± 0.57 nmol/mg whereas the glutamate concentration of benign samples was 1.32 ± 0.35 nmol/mg ($p > 0.05$).

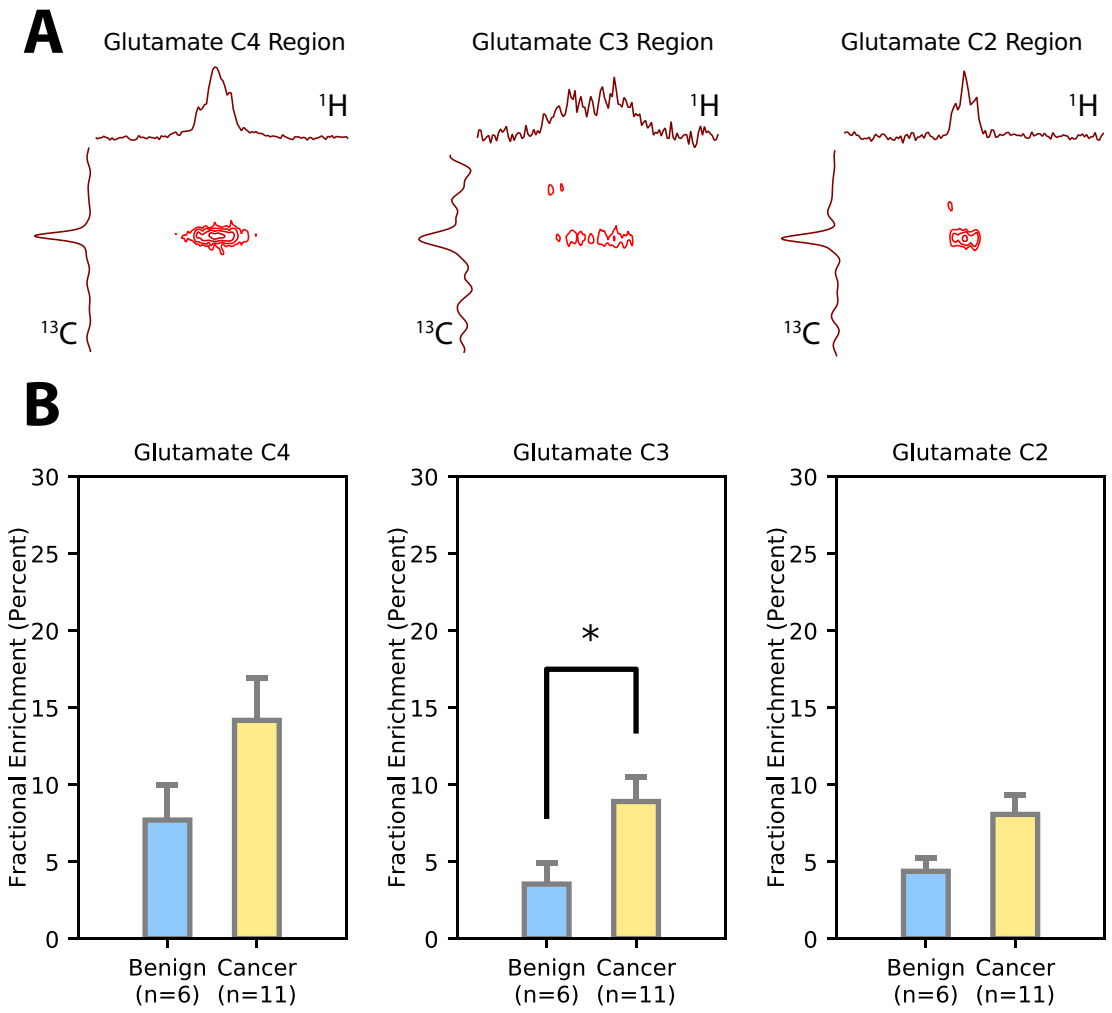

Figure 4.3. Labeling of glutamate from [1,6-$^{13}C_2$]glucose. (A) Representative HSQC spectra with 1D slices taken through the glutamate peaks. A small amount of glutamine is visible adjacent to glutamate. (B) Fractional enrichment.

Labeling of glutamate from [3-^{13}C]glutamine. Figure 4.4A shows representative HSQC peaks for glutamate C4, C3, and C2 from a cancer sample labeled with [3-^{13}C]glutamine. As shown in Figure 4.4B, we did not observe significantly increased

glutamate fractional enrichment for cancer samples labeled with [3-^{13}C]glutamine as compared to benign samples (glutamate C3: 26 ± 2 % vs. 21 ± 2 %, p = 0.15; glutamate C2: 5 ± 1 % vs. 4 ± 1 %, p = 0.20). For the samples labeled with [3-^{13}C]glutamine, we did not observe statistically significant differences between cancer and benign samples in terms of glutamate concentration after culture.

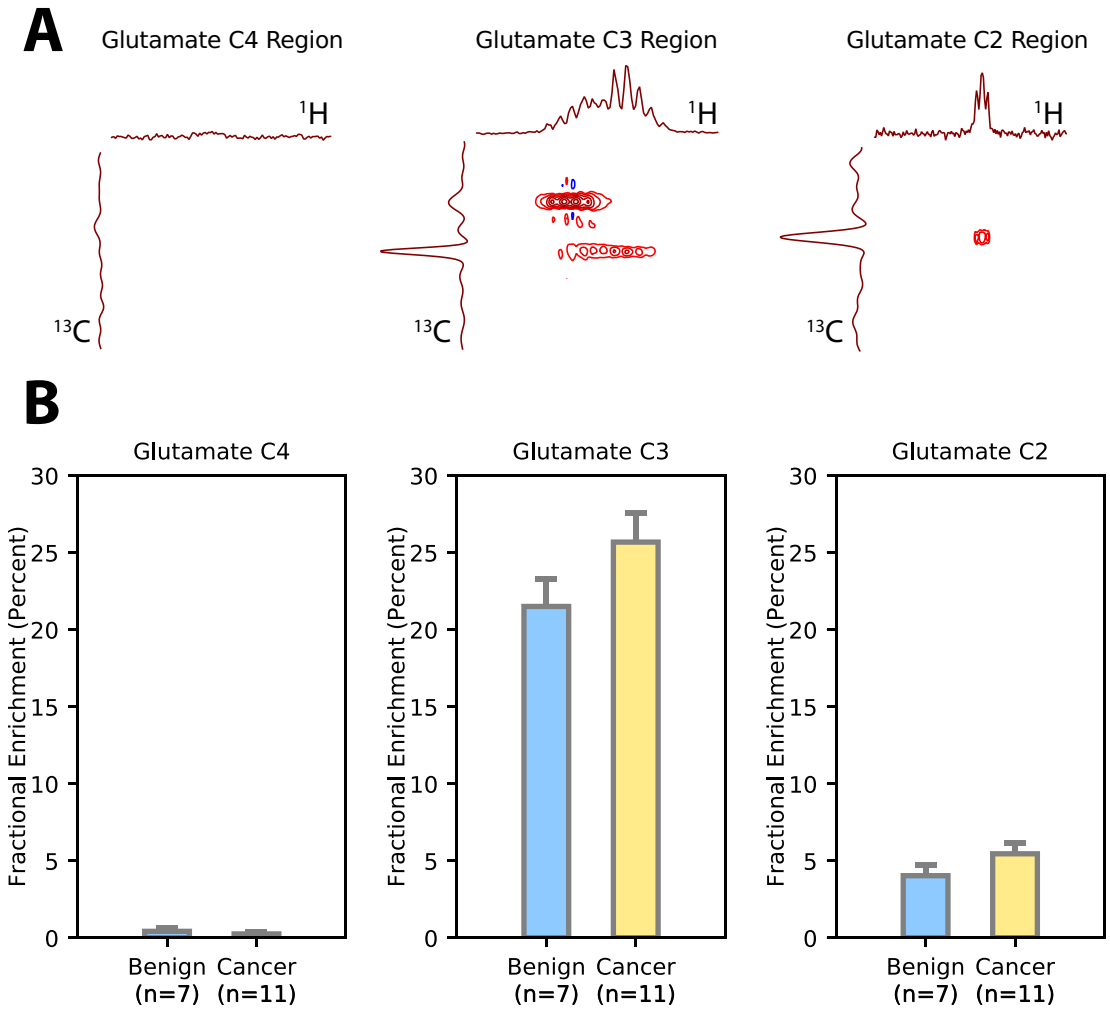

Figure 4.4. Labeling of glutamate from [3-^{13}C]glutamine. (A) Representative HSQC spectra. Glutamine C3 is visible adjacent to glutamate C3. (B) Fractional enrichment.

Oxygen consumption measurements. We obtained oxygen consumption data from n=11 living prostate tissue slices (n=8 benign slices and n=3 cancer slices). Figure 4.5A shows the custom-engineered 3D-printed holder that was used to protect the

prostate tissue slices from the magnetic stir bar during oxygen consumption measurements. The prostate tissue slices were allowed to rest upon a tissue strainer mesh that was affixed between two layers of 3D-printed RC31 NanoCure material (EnvisionTEC, Inc). Figure 4.5B shows the oxygen consumption data. The mean ± standard error oxygen consumption rate was 0.19 ± 0.02 nmol/mg/min for cancer samples, compared to 0.10 ± 0.03 nmol/mg/min for benign samples (p = 0.09, t-test).

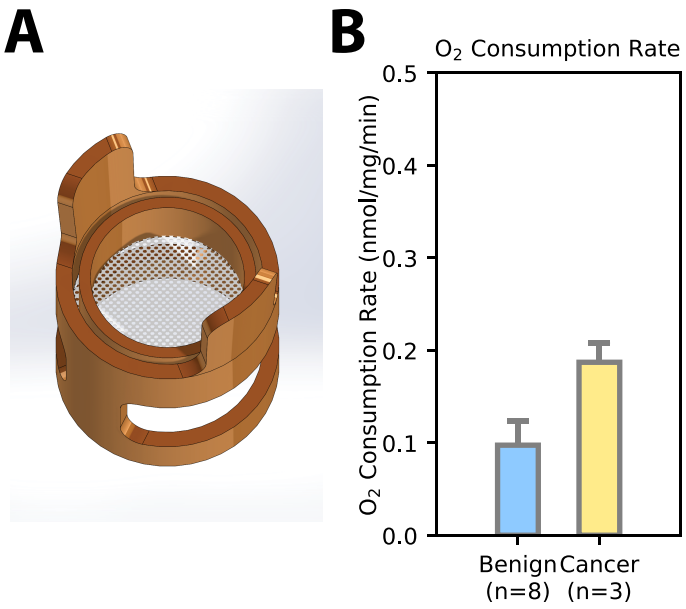

Figure 4.5. Oxygen consumption measurements in human prostate tissue. (A) 3D-printed tissue holder. (B) Oxygen consumption data.

Extended metabolic labeling. We obtained 24-hour metabolic labeling data from n=3 tissue slices (one [1,6-$^{13}C_2$]glucose labeling cancer slice and two [3-^{13}C]glutamine labeling cancer slices). Although the limited number of samples precluded statistical analysis, the fractional enrichment of the [1,6-$^{13}C_2$]glucose labeling cancer slice was similar to the fractional enrichment of the 8-hour samples. For the [3-^{13}C]glutamine labeling cancer slices, there was a modest trend towards higher fractional enrichment in

the 24-hour labeled samples, suggesting that incorporation of the [3-^{13}C]glutamine label into glutamate might not be completed after 8 hours.

Table 4.2. Comparison of tissue slices labeled for either 8 or 24 hours.

[1,6-$^{13}C_2$]glucose labeling				
Metabolite	**Carbon**	**FE % (Benign, 8 hours)**	**FE % (Cancer, 8 hours)**	**FE % (Cancer, 24 hours)**
Alanine	C3	8 ± 3	14 ± 2	8
Lactate	C3	42 ± 7	53 ± 4	52
Glutamate	C2	4 ± 1	8 ± 1	4
Glutamate	C3	4 ± 1	9 ± 2	3
Glutamate	C4	8 ± 2	14 ± 3	6
[3-^{13}C]glutamine labeling				
Metabolite	**Carbon**	**FE % (Benign, 8 hours)**	**FE % (Cancer, 8 hours)**	**FE % (Cancer, 24 hours)**
Glutamate	C2	4 ± 1	5 ± 1	11
Glutamate	C3	21 ± 2	26 ± 2	36

Discussion

To our knowledge, glutamine metabolism has not previously been directly measured in benign and malignant living human prostate tissue. In this study, we found that living human prostate tissue readily produces [3-^{13}C]glutamate from [3-^{13}C]glutamine, reflecting transamination. We additionally witnessed the production of [2-^{13}C]glutamate, (Figure 4.4) reflecting oxidative tricarboxylic acid (TCA) cycle metabolism of glutamine (Figure 4.1). These results are consistent with prior studies documenting high levels of the neutral amino acid transporter ASCT2 in benign and malignant prostate tissue,[91,92] which is believed to play a key role in glutamine uptake.[93]

We observed a slight trend towards increased fractional enrichment of glutamate coming from [3-^{13}C]glutamine in prostate cancer tissue compared to benign prostate tissue, but this trend did not reach statistical significance (Figure 4.4). Our cancer tissue

dataset comprised primarily Gleason score = 7 samples, making it impossible to draw conclusions regarding aggressive prostate cancer tissues such as NEPC and/or CRPC tumors, including tumors having Myc amplification. Thus, having established this baseline measurement of glutamine metabolism in normal human prostate tissue and in human prostate cancer, we will investigate the glutamine metabolic phenotype of aggressive prostate cancer in future studies.

In this study, we further investigated the role of glucose metabolism in prostate cancer via labeling studies performed with [1,6-$^{13}C_2$]glucose. We observed modestly higher alanine and lactate fractional enrichment in human prostate cancer compared to normal human prostate tissue, but this trend did not reach statistical significance (Figure 4.2). Looking at the TCA cycle metabolism of glucose, we observed a statistically significant increase of fractional enrichment at the glutamate C3 position in prostate cancer vs. normal samples, supported by similar (yet not statistically significant) trends at the glutamate C4 and C2 positions (Figure 4.3). (We did not correct the statistical tests of these measurements for multiple comparisons of independent samples, due to the expectation that fractional enrichments within the same metabolic pathway would be highly correlated.) These observations were supported by a trend towards higher oxygen consumption rates in prostate cancer tissues compared to normal prostate (Figure 4.5). Taken together, these results are compatible with prior thinking on the role of increased glucose metabolism and TCA cycle activity in prostate cancer.[17,94]

In prior studies from our laboratory, the fractional enrichments of alanine, lactate, and glutamate were measured in human prostate tissue slices cultures[17] and in primary cultured prostate cancer cells.[65] Due to the fact that these studies employed [3-

^{13}C]pyruvate as the metabolic labeling substrate in conjunction with unlabeled glucose for a labeling time of either one[65] or two[17] hours, the fractional enrichment values reported in these studies are not directly comparable to the present work, which employed either [1,6-$^{13}C_2$]glucose or [3-^{13}C]glutamine for a labeling time of eight hours.

For this study, given the limited sensitivity of the NMR technique and the limited availability of human prostate tissue, we chose to label the prostate tissue slices with either [1,6-$^{13}C_2$]glucose or [3-^{13}C]glutamine because these substrates produced carbon singlets that facilitated easy identification within the tissue HR-MAS HSQC spectra. However, a disadvantage of this approach was that it did not enable full specification of metabolic fluxes, which requires uniformly labeled substrates and isotopomer identification.[95] Instead, we computed fractional enrichment values, which can potentially be confounded by effects such as the overall metabolite pool sizes and various intersecting pathways.

The conclusions of this study were somewhat limited due to the cancer dataset comprising primarily Gleason score = 7 samples, as well as the moderate dataset size of 35 prostate tissue slices from five patients. Thus, in the future we plan to expand this work to include living tissue samples of aggressive human prostate cancer.

References

1. ACS. Cancer Facts and Figures 2018 [Internet]. cancer.org. [cited 2018 Dec 1]. Available from: https://www.cancer.org/research/cancer-facts-statistics/all-cancer-facts-figures/cancer-facts-figures-2018.html
2. Klotz L, Vesprini D, Sethukavalan P, Jethava V, Zhang L, Jain S, et al. Long-Term Follow-Up of a Large Active Surveillance Cohort of Patients With Prostate Cancer. Journal of Clinical Oncology. American Society of Clinical Oncology; 2014 Dec 15;33(3):JCO.2014.55.1192–277.
3. Tosoian JJ, Mamawala M, Epstein JI, Landis P, Wolf S, Trock BJ, et al. Intermediate and Longer-Term Outcomes From a Prospective Active-Surveillance Program for Favorable-Risk Prostate Cancer. Journal of Clinical Oncology. American Society of Clinical Oncology; 2015 Aug 31;33(30):JCO.2015.62.5764–3385.
4. Klein EA, Cooperberg MR, Magi-Galluzzi C, et al. A 17-gene Assay to Predict Prostate Cancer Aggressiveness in the Context of Gleason Grade Heterogeneity, Tumor Multifocality, and Biopsy Undersampling. *European Urology*. 2014;66(3):550-560. doi:10.1016/j.eururo.2014.05.004
5. Cooperberg M, Pasta D, Elkin E, Et Al. The University Of California, San Francisco Cancer Of The Prostate Risk Assessment Score: A Straightforward And Reliable Preoperative Predictor Of Disease Recurrence After Radical Prostatectomy. *The Journal of Urology*. 2005;173(6):1938-1942. doi:10.1097/01.ju.0000158155.33890.e7

6. Aggarwal R, Vigneron DB, Kurhanewicz J. Hyperpolarized 1-[13C]-Pyruvate Magnetic Resonance Imaging Detects an Early Metabolic Response to Androgen Ablation Therapy in Prostate Cancer. *European Urology*. 2017;72(6):1028-1029. doi:10.1016/j.eururo.2017.07.022
7. Warburg O, Posener K, Negelein, E. Über den Stoffwechsel der Carcinomzelle. *Biochem Zeitschr* 1924;152:309-344.
8. Koppenol WH, Bounds PL, Dang CV. Otto Warburg's contributions to current concepts of cancer metabolism. *Nat Rev Cancer*. 2011;11(5):325-337. doi:10.1038/nrc3038.
9. Ros S, Santos CR, Moco S, et al. Functional Metabolic Screen Identifies 6-Phosphofructo-2-Kinase/Fructose-2,6-Biphosphatase 4 as an Important Regulator of Prostate Cancer Cell Survival. *Cancer Discovery*. 2012;2(4):328-343. doi:10.1158/2159-8290.CD-11-0234.
10. Tessem MB, Swanson MG, Keshari KR, et al. Evaluation of lactate and alanine as metabolic biomarkers of prostate cancer using 1H HR-MAS spectroscopy of biopsy tissues. *Magn Reson Med*. 2008;60(3):510-516. doi:10.1002/mrm.21694
11. Kurhanewicz J, Vigneron DB, Brindle K, et al. Analysis of cancer metabolism by imaging hyperpolarized nuclei: prospects for translation to clinical research. *Neoplasia*. 2011;13(2):81-97. doi:10.1593/neo.101102
12. Ardenkjaer-Larsen JH, Fridlund B, Gram A, et al. Increase in signal-to-noise ratio of > 10,000 times in liquid-state NMR. *Proc Natl Acad Sci USA*. 2003;100(18):10158-10163. doi:10.1073/pnas.1733835100.

13. Chen AP, Albers MJ, Cunningham CH, et al. Hyperpolarized C-13 spectroscopic imaging of the TRAMP mouse at 3T—Initial experience. *Magn Reson Med*. 2007;58(6):1099-1106. doi:10.1002/mrm.21256.
14. Larson PEZ, Kerr AB, Chen AP, et al. Multiband excitation pulses for hyperpolarized 13C dynamic chemical-shift imaging. *Journal of Magnetic Resonance*. 2008;194(1):121-127. doi:10.1016/j.jmr.2008.06.010.
15. Albers MJ, Bok R, Chen AP, et al. Hyperpolarized 13C Lactate, Pyruvate, and Alanine: Noninvasive Biomarkers for Prostate Cancer Detection and Grading. *Cancer Research*. 2008;68(20):8607-8615. doi:10.1158/0008-5472.CAN-08-0749.
16. Larson PEZ, Hu S, Lustig M, et al. Fast dynamic 3D MR spectroscopic imaging with compressed sensing and multiband excitation pulses for hyperpolarized 13C studies. *Magn Reson Med*. 2011;65(3):610-619. doi:10.1002/mrm.22650.
17. Keshari KR, Sriram R, VanCriekinge M, et al. Metabolic Reprogramming and Validation of Hyperpolarized 13C Lactate as a Prostate Cancer Biomarker Using a Human Prostate Tissue Slice Culture Bioreactor. *Prostate*. 2013;73(11):1171-1181. doi:10.1002/pros.22665
18. Sriram R, Gordon J, Baligand C, et al. Non-Invasive Assessment of Lactate Production and Compartmentalization in Renal Cell Carcinomas Using Hyperpolarized 13C Pyruvate MRI. *Cancers 2018, Vol 10, Page 313*. 2018;10(9):313. doi:10.3390/cancers10090313.
19. Peng Y, Jiang Y, Yang C, et al. Quantitative analysis of multiparametric prostate MR images: differentiation between prostate cancer and normal tissue and

correlation with Gleason score--a computer-aided diagnosis development study. 2013;267(3):787-796. doi:10.1148/radiol.13121454.

20. Robinson D, Van Allen EM, Wu Y-M, et al. Integrative Clinical Genomics of Advanced Prostate Cancer. *Cell*. 2015;161(5):1215-1228. doi:10.1016/j.cell.2015.05.001.
21. Quigley DA, Dang HX, Zhao SG, et al. Genomic Hallmarks and Structural Variation in Metastatic Prostate Cancer. *Cell*. 2018;174(3):758-769.e759. doi:10.1016/j.cell.2018.06.039.
22. Gao P, Tchernyshyov I, Chang T-C, et al. c-Myc suppression of miR-23a/b enhances mitochondrial glutaminase expression and glutamine metabolism. *Nature*. 2009;458(7239):762-765. doi:10.1038/nature07823.
23. Dang CV. MYC on the Path to Cancer. *Cell*. 2012;149(1):22-35. doi:10.1016/j.cell.2012.03.003.
24. Abragam A, Goldman M. Principles of dynamic nuclear polarisation. *Reports on Progress in Physics*. 1978;41(3):395.
25. Kovacs H, Moskau D, Spraul M. Cryogenically cooled probes—a leap in NMR technology. *Progress in nuclear magnetic resonance spectroscopy*. 2005;46(2-3):131-155. doi:10.1016/j.pnmrs.2005.03.001.
26. Theis T, Truong ML, Coffey AM, et al. Microtesla SABRE Enables 10% Nitrogen-15 Nuclear Spin Polarization. *J Am Chem Soc*. 2015;137(4):1404-1407. doi:10.1021/ja512242d.

27. Ardenkjaer-Larsen JH, Fridlund B, Gram A, et al. Increase in signal-to-noise ratio of > 10,000 times in liquid-state NMR. *Proc Natl Acad Sci USA*. 2003;100(18):10158-10163. doi:10.1073/pnas.1733835100.
28. Ramaswamy V, Hooker JW, Withers RS, Nast RE, Brey WW, Edison AS. Journal of Magnetic Resonance. *Journal of Magnetic Resonance*. 2013;235(C):58-65. doi:10.1016/j.jmr.2013.07.012.
29. Hoult DI, Richards RE. The signal-to-noise ratio of the nuclear magnetic resonance experiment. *Journal of Magnetic Resonance (1969)*. 1976;24(1):71-85. doi:10.1016/j.jmr.2011.09.018.
30. Macovski A. Noise in MRI. *Magn Reson Med*. 1996;36(3):494-497.
31. Ocali O, Atalar E. Ultimate intrinsic signal-to-noise ratio in MRI. *Magn Reson Med*. 1998.
32. Doty FD, Entzminger G, Kulkarni J, Pamarthy K, Staab JP. Radio frequency coil technology for small-animal MRI. *NMR Biomed*. 2007;20(3):304-325. doi:10.1002/nbm.1149.
33. Capek M, Jelinek L, Hazdra P. On the Functional Relation Between Quality Factor and Fractional Bandwidth. *IEEE Trans Antennas Propagat*. 63(6):2787-2790. doi:10.1109/TAP.2015.2414472.
34. Kajfez D, HWAN HJ. Q-factor measurement with network analyzer. *IEEE transactions on microwave theory and techniques*. 1984;32(7):666-670.
35. Swanson MG, Zektzer AS, Tabatabai ZL, et al. Quantitative analysis of prostate metabolites using 1H HR-MAS spectroscopy. *Magn Reson Med*. 2006;55(6):1257-1264. doi:10.1002/mrm.20909.

36. Zhang X, Webb A. Design of a capacitively decoupled transmit/receive NMR phased array for high field microscopy at 14.1T. *Journal of Magnetic Resonance*. 2004;170(1):149-155. doi:10.1016/j.jmr.2004.05.004.
37. V V Krishnan NM. Radiation damping in modern NMR experiments: Progress and challenges. *Progress in nuclear magnetic resonance spectroscopy*. 2013;68:41-57. doi:10.1016/j.pnmrs.2012.06.001.
38. Götz Schlotterbeck, Alfred Ross, Remo Hochstrasser, et al. High-Resolution Capillary Tube NMR. A Miniaturized 5-µL High-Sensitivity TXI Probe for Mass-Limited Samples, Off-Line LC NMR, and HT NMR. *Anal Chem*. 2002;74(17):4464-4471. doi:10.1021/ac025556e.
39. Oto A, Kayhan A, Jiang Y, Tretiakova M, Yang C, Antic T, et al. Prostate Cancer: Differentiation of Central Gland Cancer from Benign Prostatic Hyperplasia by Using Diffusion-weighted and Dynamic Contrast-enhanced MR Imaging. Radiology. 2010 Dec;257(3):715–23.
40. Pinaquy JB, De Clermont Galleran H, Pasticier G, Rigou G, Alberti N, Hindié E, et al. Comparative effectiveness of [18F]-fluorocholine PET-CT and pelvic MRI with diffusion-weighted imaging for staging in patients with high-risk prostate cancer. Prostate. 2015 Feb 1;75(3):323–31.
41. Radtke JP, Teber D, Hohenfellner M, Hadaschik BA. The current and future role of magnetic resonance imaging in prostate cancer detection and management. Translational Andrology and Urology. 4(3):326–41.
42. Fütterer JJ, Briganti A, De Visschere P, Emberton M, Giannarini G, Kirkham A, et al. Can Clinically Significant Prostate Cancer Be Detected with Multiparametric

Magnetic Resonance Imaging? A Systematic Review of the Literature. European Urology. 2015 Dec;68(6):1045–53.

43. Tan CH, Wang J, Kundra V. Diffusion weighted imaging in prostate cancer. *Eur Radiol*. 2010;21(3):593-603. doi:10.1007/s00330-010-1960-y.
44. Jacobs MA, Ouwerkerk R, Petrowski K, Macura KJ. Diffusion-Weighted Imaging With Apparent Diffusion Coefficient Mapping and Spectroscopy in Prostate Cancer. *Topics in Magnetic Resonance Imaging*. 2008;19(6):261-272. doi:10.1097/RMR.0b013e3181aa6b50.
45. Zelhof B, Lowry M, Rodrigues G, Kraus S, Turnbull L. Description of magnetic resonance imaging-derived enhancement variables in pathologically confirmed prostate cancer and normal peripheral zone regions. *BJU International*. 2009;104(5):621-627. doi:10.1111/j.1464-410X.2009.08457.x.
46. Nagarajan R, Margolis D, Raman S, et al. Correlation of Gleason Scores with Diffusion-Weighted Imaging Findings of Prostate Cancer. *Advances in Urology*. 2012;2012(2):1-5. doi:10.1155/2012/374805.
47. Fan X, Haney CR, Agrawal G, et al. High-resolution MRI of excised human prostate specimens acquired with 9.4T in detection and identification of cancers: Validation of a technique. *J Magn Reson Imaging*. 2011;34(4):956-961. doi:10.1002/jmri.22745.
48. Bourne RM, Kurniawan N, Cowin G, et al. Microscopic diffusivity compartmentation in formalin-fixed prostate tissue. *Magn Reson Med*. 2012;68(2):614-620. doi:10.1002/mrm.23244.

49. Bourne RM, Kurniawan N, Cowin G, et al. Biexponential diffusion decay in formalin-fixed prostate tissue: Preliminary findings. *Magn Reson Med*. 2012;68(3):954-959. doi:10.1002/mrm.23291.
50. Einstein A. Investigations on the Theory of the Brownian Movement. *Ann der Physik (1905)*. doi:10.1234/12345678.
51. Dix JA, Verkman AS. Crowding effects on diffusion in solutions and cells. *Annu Rev Biophys*. 2008;37(1):247-263. doi:10.1146/annurev.biophys.37.032807.125824.
52. Stejskal EO, Tanner JE. Spin Diffusion Measurements: Spin Echoes in the Presence of a Time-Dependent Field Gradient. *The Journal of Chemical Physics*. 2004;42(1):288-292. doi:10.1063/1.1695690.
53. Le Bihan D, Breton E, Lallemand D, Grenier P. MR imaging of intravoxel incoherent motions: application to diffusion and perfusion in neurologic disorders. 1986.
54. van Gelderen P, de Vleeschouwer MHM, DesPres D, Pekar J, Van Zijl PCM, Moonen CTW. Water diffusion and acute stroke. *Magn Reson Med*. 1994;31(2):154-163. doi:10.1002/mrm.1910310209.
55. McNeal JE. Normal histology of the prostate. *Am J Surg Pathol*. 1988;12(8):619-633.
56. Le Bihan D, Breton E, Lallemand D, Aubin ML, Vignaud J, Laval-Jeantet M. Separation of diffusion and perfusion in intravoxel incoherent motion MR imaging. *Radiology*. 1988;168(2):497-505. doi:10.1148/radiology.168.2.3393671.

57. Dash A, Maine IP, Varambally S, Shen R, Chinnaiyan AM, Rubin MA. Changes in Differential Gene Expression because of Warm Ischemia Time of Radical Prostatectomy Specimens. *The American Journal of Pathology*. 2002;161(5):1743-1748. doi:10.1016/S0002-9440(10)64451-3.
58. Bourne R, Bongers A, Charles N, Power C, Sved P, Watson G. Effect of formalin fixation on biexponential modeling of diffusion decay in prostate tissue. *Magn Reson Med*. 2013;70(4):1160-1166. doi:10.1002/mrm.24549.
59. Jung AJ, Westphalen AC, Kurhanewicz J, et al. Clinical utility of endorectal MRI-guided prostate biopsy: Preliminary experience. *J Magn Reson Imaging*. 2014;40(2):314-323. doi:10.1002/jmri.24383.
60. Maund SL, Nolley R, Peehl DM. Optimization and comprehensive characterization of a faithful tissue culture model of the benign and malignant human prostate. *Lab Invest*. 2013;94(2):208-221. doi:10.1038/labinvest.2013.141
61. Peehl DM, Stamey TA. Growth responses of normal, benign hyperplastic, and malignant human prostatic epithelial cells in vitro to cholera toxin, pituitary extract, and hydrocortisone. Prostate. 1986;8(1):51-61. doi:10.1002/pros.2990080107
62. Nelson SJ, Kurhanewicz J, Vigneron DB, et al. Metabolic Imaging of Patients with Prostate Cancer Using Hyperpolarized [1-13C]Pyruvate. *Science Translational Medicine*. 2013;5(198):198ra108-198ra108. doi:10.1126/scitranslmed.3006070

63. Day SE, Kettunen MI, Gallagher FA, et al. Detecting tumor response to treatment using hyperpolarized 13C magnetic resonance imaging and spectroscopy. 2007;13(11):1382-1387. doi:10.1038/nm1650.
64. Comment A, Merritt ME. Hyperpolarized Magnetic Resonance as a Sensitive Detector of Metabolic Function. *Biochemistry*. 2014;53(47):7333-7357. doi:10.1021/bi501225t
65. Levin YS, Albers MJ, Butler TN, Spielman D, Peehl DM, Kurhanewicz J. Methods for metabolic evaluation of prostate cancer cells using proton and 13C HR-MAS spectroscopy and [3-13C] pyruvate as a metabolic substrate. *Magn Reson Med*. 2009;62(5):1091-1098. doi:10.1002/mrm.22120.
66. Albers MJ, Butler TN, Rahwa I, et al. Evaluation of the ERETIC method as an improved quantitative reference for 1H HR-MAS spectroscopy of prostate tissue. *Magn Reson Med*. 2009;61(3):525-532. doi:10.1002/mrm.21808
67. Shaka AJ, Barker PB, Freeman R. Computer-optimized decoupling scheme for wideband applications and low-level operation. *Journal of Magnetic Resonance (1969)*. 1985;64(3):547-552. doi:10.1016/0022-2364(85)90122-2.
68. Carlos Cobas J, Bernstein MA, Martín-Pastor M, Tahoces PG. A new general-purpose fully automatic baseline-correction procedure for 1D and 2D NMR data. *Journal of Magnetic Resonance*. 2006;183(1):145-151. doi:10.1016/j.jmr.2006.07.013.
69. Johnson S, Rabinovitch P. Ex Vivo Imaging of Excised Tissue Using Vital Dyes and Confocal Microscopy. *Current Protocols in Cytometry*. 2012;61(1):9.39.1-9.39.18. doi:10.1002/0471142956.cy0939s61

70. Keshari KR, Tsachres H, Iman R, et al. Correlation of phospholipid metabolites with prostate cancer pathologic grade, proliferative status and surgical stage – impact of tissue environment. Jagannathan NR, Bhujwalla ZM, eds. *NMR Biomed*. 2011;24(6):691-699. doi:10.1002/nbm.1738.
71. Eidelman E, Twum-Ampofo J, Ansari J, Siddiqui MM. The Metabolic Phenotype of Prostate Cancer. *Front Oncol*. 2017;7:806. doi:10.3389/fonc.2017.00131.
72. Choi SYC, Xue H, Wu R, et al. The MCT4 Gene: A Novel, Potential Target for Therapy of Advanced Prostate Cancer. *Clin Cancer Res*. 2016;22(11):2721-2733. doi:10.1158/1078-0432.CCR-15-1624.
73. Pértega-Gomes N, Vizcaíno JR, Miranda-Gonçalves V, et al. Monocarboxylate transporter 4 (MCT4) and CD147 overexpression is associated with poor prognosis in prostate cancer. *BMC Cancer*. 2011;11(1):519. doi:10.1186/1471-2407-11-312.
74. Gomes NP, Felisbino S, Massie CE, et al. A glycolytic phenotype is associated with prostate cancer progression and aggressiveness: a role for monocarboxylate transporters as metabolic targets for therapy. *The Journal of Pathology*. 2015;236(4):517-530. doi:10.1002/path.4547.
75. Hao J, Chen H, Madigan MC, et al. Co-expression of CD147 (EMMPRIN), CD44v3-10, MDR1 and monocarboxylate transporters is associated with prostate cancer drug resistance and progression. *British Journal of Cancer 2010 103:7*. 2010;103(7):1008-1018. doi:10.1038/sj.bjc.6605839.
76. Schiebler ML, Miyamoto KK, White M, Maygarden SJ, Mohler JL. In vitro high resolution 1H-spectroscopy of the human prostate: Benign prostatic hyperplasia,

normal peripheral zone and adenocarcinoma. *Magn Reson Med*. 1993;29(3):285-291. doi:10.1002/mrm.1910290302.

77. Yu EY, Gulati R, Telesca D, et al. Duration of First Off-Treatment Interval Is Prognostic for Time to Castration Resistance and Death in Men With Biochemical Relapse of Prostate Cancer Treated on a Prospective Trial of Intermittent Androgen Deprivation. *Journal of Clinical Oncology*. 2010;28(16):2668-2673. doi:10.1200/JCO.2009.25.1330.
78. James ND, de Bono JS, Spears MR, et al. Abiraterone for Prostate Cancer Not Previously Treated with Hormone Therapy. *N Engl J Med*. 2017;377(4):338-351. doi:10.1056/NEJMoa1702900.
79. Hussain M, Fizazi K, Saad F, et al. Enzalutamide in Men with Nonmetastatic, Castration-Resistant Prostate Cancer. *N Engl J Med*. 2018;378(26):2465-2474. doi:10.1056/NEJMoa1800536.
80. Smith MR, Saad F, Chowdhury S, et al. Apalutamide Treatment and Metastasis-free Survival in Prostate Cancer. *N Engl J Med*. 2018;378(15):1408-1418. doi:10.1056/NEJMoa1715546.
81. Ciarlo M, Benelli R, Barbieri O, et al. Regulation of neuroendocrine differentiation by AKT/hnRNPK/AR/β-catenin signaling in prostate cancer cells. *International Journal of Cancer*. 2012;131(3):582-590. doi:10.1002/ijc.26402.
82. Aggarwal R, Zhang T, Small EJ, Armstrong AJ. Neuroendocrine prostate cancer: subtypes, biology, and clinical outcomes. *J Natl Compr Canc Netw*. 2014;12(5):719-726.

83. Li Y, Donmez N, Sahinalp C, et al. SRRM4 Drives Neuroendocrine Transdifferentiation of Prostate Adenocarcinoma Under Androgen Receptor Pathway Inhibition. *European Urology*. 2017;71(1):68-78. doi:10.1016/j.eururo.2016.04.028.
84. Kurhanewicz J, Vigneron DB, Ardenkjaer-Larsen JH, et al. Hyperpolarized 13C MRI: Path to Clinical Translation in Oncology. *Neoplasia*. 2019;21(1):1-16. doi:10.1016/j.neo.2018.09.006.
85. Priolo C, Pyne S, Rose J, et al. AKT1 and MYC Induce Distinctive Metabolic Fingerprints in Human Prostate Cancer. *Cancer Research*. 2014;74(24):7198-7204. doi:10.1158/0008-5472.CAN-14-1490.
86. Choi SYC, Ettinger SL, Lin D, et al. Targeting MCT4 to reduce lactic acid secretion and glycolysis for treatment of neuroendocrine prostate cancer. *Cancer Medicine*. 2018;7(7):3385-3392. doi:10.1002/cam4.1587.
87. Deelchand DK, Ugurbil K, Henry P-G. Investigating brain metabolism at high fields using localized 13C NMR spectroscopy without 1H decoupling. *Magn Reson Med*. 2006;55(2):279-286. doi:10.1002/mrm.20756.
88. Sami Heikkinen, Merja M Toikka, Pirkko T Karhunen A, Ilkka A Kilpeläinen. Quantitative 2D HSQC (Q-HSQC) via Suppression of J-Dependence of Polarization Transfer in NMR Spectroscopy: Application to Wood Lignin. *J Am Chem Soc*. 2003;125(14):4362-4367. doi:10.1021/ja029035k.
89. Peterson DJ, Loening NM. QQ-HSQC: a quick, quantitative heteronuclear correlation experiment for NMR spectroscopy. *Magn Reson Chem*. 2007;45(11):937-941. doi:10.1002/mrc.2073.

90. Mandal PK, Majumdar A. A comprehensive discussion of HSQC and HMQC pulse sequences. *Concepts in Magnetic Resonance Part A*. 2004;20A(1):1-23. doi:10.1002/cmr.a.10095.
91. Li R, Younes M, Frolov A, et al. Expression of neutral amino acid transporter ASCT2 in human prostate. *Anticancer Res*. 2003;23(4):3413-3418.
92. Wang Q, Hardie RA, Hoy AJ, et al. Targeting ASCT2-mediated glutamine uptake blocks prostate cancer growth and tumour development. *The Journal of Pathology*. 2015;236(3):278-289. doi:10.1002/path.4518.
93. Wise DR, Thompson CB. Glutamine addiction: a new therapeutic target in cancer. *Trends in Biochemical Sciences*. 2010;35(8):427-433. doi:10.1016/j.tibs.2010.05.003.
94. Franklin RB, Milon B, Feng P, Costello LC. Zinc and zinc transporters in normal prostate and the pathogenesis of prostate cancer. *Front Biosci*. 2005;10:2230-2239.
95. Forbes NS, Meadows AL, Clark DS, Blanch HW. Estradiol stimulates the biosynthetic pathways of breast cancer cells: Detection by metabolic flux analysis. *Metabolic Engineering*. 2006;8(6):639-652. doi:10.1016/j.ymben.2006.06.005.

Publishing Agreement

It is the policy of the University to encourage the distribution of all theses, dissertations, and manuscripts. Copies of all UCSF theses, dissertations, and manuscripts will be routed to the library via the Graduate Division. The library will make all theses, dissertations, and manuscripts accessible to the public and will preserve these to the best of their abilities, in perpetuity.

Please sign the following statement:

I hereby grant permission to the Graduate Division of the University of California, San Francisco to release copies of my thesis, dissertation, or manuscript to the Campus Library to provide access and preservation, in whole or in part, in perpetuity.

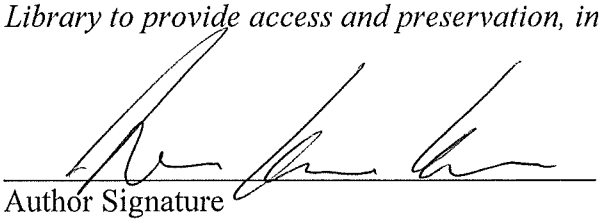

Author Signature

12/21/2018

Date